Attenuated activation of pulmonary immune cells in mRNA-1273 vaccinated hamsters after SARS-CoV-2 infection

Michelle Meyer[1,2*], Yuan Wang[3,4*], Darin Edwards[5*], Gregory R. Smith[6*], Aliza B. Rubenstein[6*], Palaniappan Ramanathan[1,2*], Chad E. Mire[2,7], Colette Pietzsch[1,2], Xi Chen[4,8], Yongchao Ge[6], Wan Sze Cheng[6], Carole Henry[5], Angela Woods[5], LingZhi Ma[5], Guillaume B. E. Stewart-Jones[5], Kevin W. Bock[9], Mahnaz Minai[9], Bianca M. Nagata[9], Sivakumar Periasamy[1,2], Pei-Yong Shi[10], Barney S. Graham[11], Ian N. Moore[9], Irene Ramos[6], Olga G. Troyanskaya[3,4,8], Elena Zaslavsky[6], Andrea Carfi[5#], Stuart C. Sealfon[6#], Alexander Bukreyev[1,2,7#]

[1] Department of Pathology, University of Texas Medical Branch, Galveston, TX 77555

[2] Galveston National Laboratory, Galveston, TX 77555

[3] Department of Computer Science, Princeton University, Princeton NJ 08540

[4] Lewis-Sigler Institute of Integrative Genomics, Princeton University, Princeton NJ 08540

[5] Moderna Inc, Cambridge, MA, 02139

[6] Department of Neurology, Icahn School of Medicine at Mount Sinai, New York, NY 10029

[7] Department of Microbiology & Immunology, University of Texas Medical Branch, Galveston, TX 77555

[8] Center for Computational Biology, Flatiron Institute, Simons Foundation, New York, NY 10010

[9] Infectious Disease Pathogenesis Section, Comparative Medicine Branch, National Institute of Allergy and Infectious Diseases, National Institutes of Health, Rockville, MD 20852

[10] Department of Biochemistry and Molecular Biology, University of Texas Medical Branch,

Galveston, TX 77555

[11] Vaccine Research Center, National Institute of Allergy and Infectious Diseases, National Institutes of Health, Bethesda, MD 20892

* These authors contributed equally

#Address correspondence to:

Andrea Carfi, Moderna Inc, Cambridge, MA 02139; Phone: 617-335-7307; Email: andrea.carfi@modernatx.com

Stuart C. Sealfon, Icahn School of Medicine at Mount Sinai, New York, NY 10029, USA. Phone: 212-241-7327; E-mail: stuart.sealfon@mssm.edu.

Alexander Bukreyev, Departments of Pathology and Microbiology & Immunology, Galveston National Laboratory, University of Texas Medical Branch, Galveston, Texas 77555-0609, USA. Phone: 409-772-2829; E-mail: alexander.bukreyev@utmb.edu.

ABSTRACT

The mRNA-1273 vaccine was determined to be effective against severe acute respiratory syndrome coronavirus 2 (SARS-CoV-2) from interim Phase 3 results and subsequently received an emergency use authorization by the FDA. Human studies, however, cannot provide the controlled response to infection and complex immunological insight that are only possible with preclinical studies. Hamsters are the only model that reliably exhibit severe SARS-CoV-2 disease similar to hospitalized patients, making them pertinent for vaccine evaluation. We demonstrate that prime or prime-boost administration of mRNA-1273 in hamsters elicited robust neutralizing antibodies, ameliorated weight loss, suppressed SARS-CoV-2 replication in the airways, and better protected against disease at the highest prime-boost dose. Unlike in mice and non-human primates, low level virus replication in mRNA-1273 vaccinated hamsters coincided with an anamnestic response. Single-cell RNA sequencing of lung tissue permitted high resolution analysis which is not possible in vaccinated humans. mRNA-1273 prevented inflammatory cell infiltration and the reduction of lymphocyte proportions, but enabled antiviral responses conducive to lung homeostasis. Surprisingly, infection triggered transcriptome programs in some types of immune cells from vaccinated hamsters that were shared, albeit attenuated, with mock-vaccinated hamsters. Our results support the use of mRNA-1273 in a two-dose schedule and provide insight into the potential responses within the lungs of vaccinated humans who are exposed to SARS-CoV-2.

INTRODUCTION

When the World Health Organization declared SARS-CoV-2 a global pandemic in March 2020, Phase 1 clinical trials on the most promising vaccine candidates had already commenced. Nucleoside modified mRNA, a relatively new addition to the arsenal of vaccine platforms, has shown promise against numerous viral infectious diseases in preclinical trials (1, 2), and phase 1

and 2 trials that are completed (3, 4) or currently underway (5-7). Previous preclinical work on a related betacoronavirus enabled the rapid development of mRNA-1273, a vaccine composed of a modified mRNA encoding for a stabilized prefusion form of the SARS-CoV-2 spike (S) protein encapsulated in lipid nanoparticles (1). Vaccination with mRNA-1273 significantly reduced infection in the lungs and upper airways of mice (1) and rhesus macaques (8). In phase 1 (9, 10) and phase 2 studies the vaccine was found to be safe and to elicit robust neutralizing antibody responses. More recently, interim analysis of Phase 3 data indicated mRNA-1273 was 94.1% efficacious in prevention of COVID-19 disease and highly efficacious in protecting against severe disease (11). On December 18, 2020, the U.S. Food and Drug Administration authorized the emergency use of mRNA-1273.

Nonhuman primate (12-14), ferret (15-17) and mouse (18) models that have been developed to understand SARS-CoV-2 pathogenesis and test vaccine and therapeutics efficacies display a mild course of disease. The lack of overt symptoms in NHPs and ethical constraints due to the sheer numbers required to recapitulate low frequency human cases with severe clinical manifestations limits the ability to understand all aspects of the disease and vaccine effectiveness. Hamsters are highly susceptible to SARS-CoV-2 and develop a severe pneumonia similar to COVID-19 patients (19-22). Hamster angiotensin converting enzyme – 2 (ACE2) receptors, that enable SARS-CoV-2 binding and entry, are analogous to the human receptor (20) and therefore, virus adaptation (18) or transgenic modifications (23) are not required for permissiveness. Additionally, hamsters can support high levels of virus replication and transmission, demonstrate weight loss and lethality with high SARS-CoV-2 infectious doses (21), making them an ideal model for evaluating vaccines.

Here, we tested the efficacy of the mRNA-1273 vaccine with prime only and three dose levels of prime-boost regimens using the stringent golden Syrian hamster model. Serological, virological, clinico-pathological and single cell (sc) RNA-seq analyses were conducted to characterize

vaccine-mediated immunity before and after challenge. We show that vaccination induced robust virus neutralizing antibody responses, attenuated virus replication, and mitigated against the influx of inflammatory innate immune cells and the relative reduction of lymphocytes in the lungs after challenge, although activated immune cell populations were observed. Our data illustrates the viral, cellular, and immune dynamics within the lungs of vaccinated hamsters which may offer a unique perspective into the events which occur within the lungs of vaccinated humans who are exposed to SARS-CoV-2.

RESULTS

Vaccination induces potent antibody responses

Three groups of outbred hamsters (*n* = 15) were vaccinated with 25 μg, 5 μg and 1 μg of mRNA-1273 via the intramuscular (IM) route in a prime (week 0)-boost (week 3) regimen (Figure 1A). One group of hamsters (*n* =15) received a prime-only dose of 25 μg at week 0 and another group (*n* =15) were mock vaccinated as the study's control. The humoral responses to vaccination were measured by enzyme-linked immunosorbent assay (ELISA) specific for the SARS-CoV-2 S protein (Figure 1B) and its receptor binding domain (RBD; Figure 1C). Three weeks after the prime dose, higher S-specific IgG titers were detected in hamsters vaccinated with 25 μg and 5 μg doses compared to the 1 μg dose (Figure 1B). S-specific IgG titers were significantly augmented in all groups following the booster, but continued to be significantly higher in the 25 μg and 5 μg dose groups compared to 1 μg dose group. RBD-specific IgG titers were comparable among hamsters in the prime-boost regimen groups after receipt of their first dose (Figure 1C). After a boost dose, RBD titers had increased significantly (P<0.0001) and remained comparable among the prime-boost groups. RBD titers in the prime-boost vaccine groups were also significantly higher after the second dose when compared to the 25 μg prime-only group (P<0.0001), while titers remained unchanged for the 25 μg prime-only group between weeks 3

and 6 post-vaccination. The ability of serum to neutralize live SARS-CoV-2 reporter virus was also determined (Figure 1D, Supplemental Methods). Most vaccinated hamsters produced neutralizing titers after the prime dose. As with RBD-binding titers, neutralizing titers significantly increased in all groups which received a booster dose, and the levels remained comparable among these hamster groups, but higher versus the prime-only vaccine group. The magnitude of neutralizing antibody titers in all booster-vaccinated groups was higher than in convalescent COVID-19 patients, while titers in the prime-only group were comparable to those seen in these subjects. Neutralizing titers significantly correlated with S-specific IgG titers (Supplemental Figure 1A) and RBD-specific titers (Supplemental Figure 1B), albeit the correlation was greater with RBD-specific IgG titers at both weeks 3 and 6 post-vaccination.

Prime-boost vaccination effectively protects against SARS-CoV-2 replication in the lungs

Six weeks after prime vaccination (3 weeks after the boost vaccination), all treatment group hamsters were challenged intranasally with 10^5 plaque forming units (PFU) of SARS-CoV-2. Hamsters were monitored daily for changes in body weight. At 2 and 4 days post infection (dpi), 5 animals from each group were serially euthanized, and the viral load in the right lung and nasal turbinates was determined. The remaining hamsters were observed until the study's endpoint at day 14. Mock vaccinated hamsters lost an average maximum body weight of 12% by day 6 (Figure 2A and Supplemental Figure 2, A and B). The prime-boost regimen prevented significant weight loss for all but one hamster in the 5 μg prime-boost group; excluding animals necropsied at 2 and 4 dpi, the average maximum weight loss for the combined prime-boost dose vaccine groups was 2.25% over the 14 day infection period (Supplemental Figure 2B). The prime-only vaccinated group lost a maximal mean weight of 6.2%. Moderate inverse correlations were observed between maximum percent weight loss and S-binding IgG and neutralizing antibody titers at week 6 (Supplemental Figure 3A).

At 2 dpi, high viral loads were detected by plaque assay in the lungs and nasal turbinates of the mock vaccinated group with a peak mean of 6.8 $\log_{10}$ PFU/g and 6.9 $\log_{10}$ PFU/g, respectively (Figure 2B). Markedly lower levels of virus were detected in the lungs of all vaccinated groups, while the 1 μg prime-boost dose group had no detectable virus in the lungs. The mean peak virus load in the nasal turbinates were similar among the prime-boost groups and 4.3 $\log_{10}$ lower compared to the mock (P<0.0001). At 4 dpi, there was no detectable virus in the lungs and nasal turbinates of all prime-boost recipients. Hamsters that received the prime-only vaccine dose had 4.8 $\log_{10}$ and 3.0 $\log_{10}$ reductions of peak virus load means, respectively, in the lungs and nasal turbinates compared to the control group. At 14 dpi, no virus was detected in all groups.

We measured viral subgenomic RNA (sgRNA) in these tissues by qRT-PCR as a potential gauge for replicating virus. Peak sgRNA were detected in the mock group at 2 dpi, with geometric means of 7.4 $\log_{10}$ (95% CI range 7.0 $\log_{10}$ - 7.9 $\log_{10}$) copies/g in the lungs and 7.3 $\log_{10}$ (95% CI range 7.1 $\log_{10}$ – 7.5 $\log_{10}$) copies/g in nasal turbinates (Figure 2C). All prime-boost groups showed similar lower sgRNA levels compared to the mock vaccine group with peak geometric means of 2.1 $\log_{10}$ (95% CI range 0.86 $\log_{10}$ – 3.3 $\log_{10}$) sgRNA copies/g in lungs and 6.3 $\log_{10}$ (95% CI range 6.4 $\log_{10}$ – 6.1 $\log_{10}$) sgRNA copies/g in nasal turbinates. In the prime-only vaccine group, sgRNA levels were not significantly reduced in either of these tissues. In close agreement with viral load, no sgRNA was detected in the lungs of prime-boost groups by 4 dpi, except for one hamster in the 1 μg dose group. While viral load was not detected in the nasal turbinates of prime-boost recipients, sgRNA was detected, albeit at markedly reduced levels compared to the mock-vaccinated group. SARS-CoV-2 transmission has been shown to correlate with levels of infectious virus and not sgRNA (22). Therefore, the likelihood of onward transmission was highly reduced by mRNA-1273. The prime-only dose afforded a less robust protection according to sgRNA levels, particularly in the nasal turbinates. Neutralizing antibody titers at week 6 inversely correlated with viral load and sgRNA in both the lungs and nasal turbinates at 2 and 4 dpi (Supplemental Figure

3B and C).

Fourteen days post challenge, the mock vaccinated hamsters had measurable serum S- (Supplemental Figure 4A) and nucleocapsid (NP)-specific (Supplemental Figure 4B) IgG titers and neutralizing titers (Supplemental Figure 4C). An anamnestic response was observed as soon as 4 dpi with the S-specific IgG increasing in recipients of the prime only vaccine regimen. At 14 dpi, all vaccinated hamsters displayed an anamnestic S-specific IgG antibody response. This result contrasts with the unwavering virus-specific IgG levels observed post challenge in vaccinated NHPs (8). Furthermore, NP-specific IgG titers were detected in all groups at 14 dpi (Supplemental Figure 4B) confirming, together with the detection of sgRNA in the upper and lower respiratory tract (Figure 2C), replication of the challenge virus before clearance.

High dose prime-boost vaccination protects against severe pathological changes in the lungs

The lungs of hamsters were evaluated histologically following challenge with SARS-CoV-2 at 2-, 4- and 14-day timepoints (Figure 2D, Supplemental Figure 5 and Supplemental Figure 6). A naïve group of hamsters (*n* = 4), intranasally administered media to mimic virus inoculum and euthanized 4 days later, was included as a control and presented with a moderately prominent alveolar interstitial hypercellularity. While these hypercellular areas may represent regions of atelectasis, the presence of *Pasteurella multocida,* a common respiratory commensal, was also detected by metagenomics analysis of all lung samples used in scRNA-seq (Supplemental Table 1) (24). At 2 dpi, SARS-CoV-2 infection in mock vaccinated animals caused mild interstitial inflammation in the lungs with some animals exhibiting a largely polymorphonuclear cellular infiltrate, comprised predominantly of neutrophils/heterophils, in and around the lung airways (Supplemental Figure 6 and Supplemental Table 2). By 4 dpi, inflammation was largely associated with perivascular and peribronchiolar regions in both a focally diffuse or multifocal distribution

affecting, on average, 30-50% of the lung that persisted until the study's endpoint (Figure 2D, Supplemental Figure 5, Supplemental Table 2). Over the 14-day infection course, prime-boost vaccinated animals displayed mild to moderate inflammation mostly involving the pulmonary interstitium, characterized by expanded alveolar capillary profiles, diminished alveolar spaces and influx of predominantly mononuclear cells (Figure 2D, Supplemental Figure 5, Supplemental Figure 6 and Supplemental Table 2). In the 1 μg prime-boost group, the predominant inflammatory phenotype was mild to moderate interstitial and rarely perivascular-peribronchiolar (4 dpi) inflammation. However, one animal exhibited a more severe pulmonary inflammatory response at 2 dpi, characterized by mild to moderate edema and rare foci of hemorrhage and vascular congestion that was previously described in SARS-CoV-2 infected hamsters (19). Prime-only vaccinated animals generally exhibited reduced inflammation compared to mock-vaccinated animals at 4 dpi; one outlier hamster presented mild pulmonary edema and scant fibrin deposition which was not observed in the rest of the group. Irrespective of vaccination schedule and dose, the airway lumen remained clear of inflammatory cells and cellular debris.

Lung sections were also examined for SARS-CoV-2 antigen at 4 dpi by immunohistochemistry (Figure 2D, Supplemental Figure 5, Supplemental Table 2 and Supplemental Methods). Large amounts of viral antigen were found throughout the lungs of mock-vaccinated hamsters. Prime-boost vaccination limited the amount of detectable total viral antigen more so than prime-only vaccination; SARS-CoV-2 antigen was minimal to absent in the 25 μg and 5 μg prime-boost groups.

Notably, the three outlier hamsters with more severe histopathological phenotypes identified in the 25 μg prime-only group at 4 dpi and in the 1 μg prime-boost group at 2 and 4 dpi, did not exhibit drastic weight loss. Their levels of infectious virus or sgRNA in the lungs or nasal turbinates were also comparable with other group members, with the exception of the single 1 μg recipient at 4 dpi that had detectable sgRNA in the lungs that were not detected in other prime-boost

recipients at the same time point. Both 4 dpi outliers had the highest level of viral antigen among all vaccinated hamster samples. Interestingly, all three outliers did not produce neutralizing titers after prime vaccination, a finding that suggests the importance of vaccine dose level and regimen, and the evolving immune response following administration of a second dose.

Integrated single cell analysis and cell type identification

We performed scRNA-seq on the cranial lung lobe tissue samples from three of the study's hamster groups that were euthanized at 4 dpi: the naive hamsters mock-infected with media (Naive, N, *n* = 4) and the 5 μg prime-boost vaccinated (Vaccinated + Infected, VI, *n* = 5) and mock-vaccinated (Mock-Vaccinated + Infected, MI, *n* = 5) groups infected with SARS-CoV-2. Lung samples from the N group served as a baseline control for analysis. The scRNA-seq data were aligned against the hamster and SARS-CoV-2 genomes and integrated using the Seurat scRNA-seq analysis pipeline (25). Integration of the single cell data identified 17 cell types, including multiple T cell, dendritic cell (DC) and macrophage subtypes (Figure 3A). The main markers used to distinguish the cell types are shown in Supplemental Figure 7A.

The expression profile of one VI animal (Supplemental Figure 8A) that showed excessive weight loss at 4 dpi (Supplemental Figure 2A) was very distinct and was not included in the integrated analysis. Granulocytes represented over 75% of the cells in this outlier sample but were less than 5% of cells in the other VI samples (Figure 3B). The gene expression pattern in the granulocytes from the outlier VI sample also differed from the granulocytes in the other VI samples (Supplemental Figure 8, B and C). Pathway analysis of the differentially expressed genes (DEGs) in granulocytes from the outlier showed upregulation of classical neutrophil processes associated with degranulation, activation and proliferation, and downregulation of immune suppressive interleukins (Supplemental Figure 8D).

The three groups showed distinct differences in cell-type proportions for many of the cell types (Figure 3, B and C, Supplemental Figure 7B). Notably, while interstitial macrophages constituted a negligible fraction of the total cells in N hamsters, the proportion of interstitial macrophages in MI hamsters was greater in 30% of the total cells (Figure 3, B and C). Importantly, this increase in macrophages was not seen in VI hamsters. Significant increases in the proportions of alveolar macrophages, DC subtypes (plasmacytoid DC [pDC], conventional DC [cDC] and activated DC [DCα], and granulocytes were also found in MI hamsters and not VI hamsters. In agreement with the observed cellular infiltration in MI hamsters, biomarkers of inflammation including IL-6, MCP-1 and IL-2, measured in a multiplex assay (Supplemental Methods), were significantly greater in the lungs of MI hamsters compared to N hamsters. The expression of inflammatory markers in the lungs of VI hamsters were generally low and comparable with the N hamsters (Supplemental Figure 9). We detected decreases in proportion of $CD4^+$, $CD8^+$ and $CD8^+$ activated T cells in MI hamsters and not VI hamsters (Figure 3, B and C). The MI and VI hamsters both showed increases in the proportion of the dividing immune cells and monocytes when compared to N hamsters. The moderate changes in the cell-type composition of VI hamsters and infiltration of inflammatory cells in lungs of MI hamsters are consistent with histology results described in the previous section.

Vaccination attenuates infection of immune cells and inflammation but enables recall responses

To identify the extent of infection of cell within the lungs, the scRNA-seq reads were mapped to the SARS-CoV-2 genome. Viral gene reads were detected only in MI hamsters (Figure 4A, Supplemental Figure 10, A and B), consistent with the clearance of infection in the lungs of the VI hamsters that was observed by qRT-PCR (Figure 2C). Several MI samples with higher overall viral reads had virus gene expression detected in a broad selection of cell types in the lungs,

including lymphoid and myeloid cells (Figure 4A) which is consonant with other studies sampling bronchoalveolar lavage fluid (BALF) (26), blood or post-mortem lung tissues (27, 28) from severe infections in humans. Macrophages and granulocytes had the highest average viral read counts (Supplemental Figure 10E). The relative levels of reads for viral gene segments within each lung sample was highly variable across animals (Supplemental Figure 10F). Inter-individual variation in the relative levels of viral transcripts has been previously described in cells isolated from the BALF of COVID-19 patients (29) and lung tissues from NHPs (30).

Expression of CCL8, the chemoattractant for monocytes and macrophages reported to be significantly induced in response to SARS-CoV-2 infection in ferret upper respiratory tract (17), was minimal in the lungs of N animals but most up-regulated in the MI hamsters (Figure 4B, Supplemental Figure 10C). The upregulation of CCL8 is consistent with macrophage infiltration of the lung observed in the MI group and in COVID-19 patients (31). The cellular distribution of CCL8 expression in MI lung mirrored that of the virus RNA, being highest in the interstitial and alveolar macrophage populations. In the VI group, increases in CCL8 expression was only observed in the macrophage populations in some of the samples studied, despite the absence of SARS-CoV-2 mRNA (Figure 4B, Supplemental Figure 10D). Overall, these data suggest that vaccination impedes SARS-CoV-2 infection of lymphoid and myeloid cells.

We assessed the activation states of nondividing lymphocyte cell clusters (Supplemental Figure 11) and their counterparts undergoing division (Supplemental Figure 12A and B), and compared the transcriptional changes in expression markers between N, MI and VI hamsters. All cells types assessed in both MI and VI hamsters underwent transcriptional changes signifying an activation state when compared to N hamsters. The nondividing $CD4^+$ T cells in VI hamsters had higher expression of genes representative of T helper (Th) 1 responses (*Il-2* and *Anxa1*) (32-34) and memory phenotypes (*S100a4*, *Lgals1* and *Anxa1*) than MI and N groups (Supplemental Figure 11). Nondividing $CD4^+$ T cells from MI hamsters were reduced for genes transcripts important for

survival (*Il7r*), regulation (*Socs2*) and viral clearance (*Ltb*) (35) and encoded more transcripts potentially driving proinflammatory effector functions (*Ccl5, Isg15*) (36) compared to VI and N hamsters. Among all cell types in VI hamsters, $CD4^+$ T cells was the greatest dividing cluster when compared to MI or N hamsters (Supplemental Figure 12C) that potentially enabled a rapid recall response within the lungs through augmentation of transcripts encoding cytotoxic molecules (37) and antibody binding Fc receptor (*FcerIg*) (38) and repression of transcripts responsible for migration (*S1pr1)* (39) (Supplemental Figure 12D). Additionally, transcriptional regulators *Tbx21* and *Zbtb32* that drive Th1 polarization (40) were increased in VI hamsters compared to MI and N hamsters, while *Gata3*, a Th2 marker, was reduced compared N hamsters. These data are consistent with a Th1 polarized recall response to viral challenge in the VI animals and suggests vaccine-induced $CD4^+$ T cells contributes substantially towards virus clearance.

Nondividing B cells in VI hamsters were reduced in *Ighm* transcripts compared to MI and N hamsters, indicating they were differentially class-switched away from IgM production (Supplemental Figure 11). Dividing B cells in VI hamsters had more transcripts representative of memory or plasma cells (*Ssr3* and *Mzb1*) than MI and N hamsters (Supplemental Figure 12D). The transcription repressor, *Prmd1*, was also greater in VI than MI and N hamsters and together with the *Zbtb32* repressor (41), potentially enabled differentiation of memory cells into IgG secreting plasma cells thus coinciding with the observed amnestic antibody response induced after infection. Dividing B cells in MI hamsters had more transcripts associated with inflammation (*Fos*, *Klf6*, *Zfp36* and *S100a8*) than VI or N hamsters.

Both dividing and nondividing $CD8^+$ T cells in VI hamsters possessed a lower effector and cytotoxic potential than MI hamsters (Supplemental Figure 11 and Supplemental Figure 12D). Transcripts encoding both stimulatory (*Cd27*, *Tnfrsf4* and *Tnfrsf18*) and inhibitory (*Lag3*) molecules where increased in dividing $CD8^+$ T cells in MI hamsters compared to VI and N hamsters and suggests these proliferating cells may be dysfunctional or exhausted (42, 43)

(Supplemental Figure 12D).

NK cells and their dividing counterparts in VI hamsters were enriched for *Fcerlg* and *Klrk* and the cytotoxic *Gzma* transcripts, and had reduced chemokine *Xcl1* transcripts (44) compared to MI or N hamsters, that suggest that they were active or mature (Supplemental Figure 11 and Supplemental Figure 12D). Dividing and nondividing NK cells in MI hamsters were also augmented for transcripts driving effector functions (*Ccl4* and *Ccl5* chemokines and interferon response) in addition to transcripts encoding cytotoxic granules, indicating an enhanced cytolytic potential compared to VI hamsters.

Overall, the transcriptional changes in lymphocytes from VI hamsters which occurred after infection are likely to represent memory driven responses from the adaptive arm of immunity established by mRNA-1273.

Following SARS-CoV-2 infection, similar transcriptional programs are regulated in lung immune cells from vaccinated and mock-vaccinated hamsters

To determine whether immune cells in the lungs showed differences in their transcriptional states in the three groups studied, we focused on two lymphoid cell types critical for viral clearance during respiratory infections, $CD8^+$ T cells and NK cells, which were relatively abundant across all samples. We also examined myeloid cells, including pDCs, cDCs, and monocytes. Differential expression analysis comparing the MI and VI groups for each cell type annotated for an increase in virus response and innate immune response pathways in all MI cell types (Supplemental Table 3). However, to more fully resolve the relationship of the pathways regulated in MI and VI cells, we subsequently performed differential expression analysis for each cell type (see Methods), comparing the MI to N samples and the VI to N samples. In all cell types, fewer transcripts were differentially expressed in the VI vs. N comparison than in the MI vs. N comparison; the DEGs in

VI samples were predominantly a subset of the DEGs in MI samples (Figure 5). A scatter plot comparing the log fold-changes of the set of transcripts significantly regulated (FDR <0.05) in either MI or VI comparisons to N showed that changes of these transcripts were highly correlated for MI and VI samples (p<2.2e^-16). The slope of the linear regression fit was less than 1, indicating that the gene expression changes were relatively lower in the VI samples. Overall, these results indicated that across all cell types analyzed, the transcriptome regulation in the VI group was similar but of lower magnitude in the MI group.

To elucidate the common pathways regulated in the MI and VI groups, we performed a network-based functional enrichment analysis which leverages genetic and epigenetic information from extensive public data sets pre-built specifically for the lung tissue (45). DEGs were clustered into modules according to their functional relatedness in the lung using a community clustering algorithm to capture higher-order tissue-specific genetic functions. Among the modules that show an up-regulated tendency, immune activation and viral response were noted across $CD8^+$ T cells (Figure 6A), NK cells (Figure 6B), cDC (Figure 7A), and monocytes (Figure 7B). The sensitivity for DEGs in pDCs (Supplemental Figure 13A) was limited by the number of cells captured in the N and VI samples (27 pDCs in N samples and 87 pDCs in the VI samples). Common pathway enrichment analysis could not be performed for the pDCs due to the small number of DEGs identified in the VI group.

We also performed the same type of network-based functional analysis on the DEGs that were specific to either MI or VI groups for each cell type analyzed. Similar pathways were modulated in MI-specific $CD8^+$ T cell DEGs and NK cell DEGs; viral response, migration, regulation of apoptotic signaling, and cellular responses to interferon-γ and oxidative stress were upregulated, while homeostasis and cellular maintenance were downregulated (Supplemental Figure 14A and B). However, the proliferation process was upregulated in $CD8^+$ T cells and negatively regulated in NK cells. Type I interferon production and viral response pathways were upregulated, and

cellular maintenance pathways were downregulated in MI-specific cDC DEGs and monocyte DEGs (Supplemental Figure 15A and B). Adaptive immune response, including T-cell activation, was modulated in both MI-specific cDC DEGs and MI-specific pDC DEGs (Supplemental Figures 15A and 13B). Finally, additional viral response pathways were upregulated in MI-specific pDC DEGs (Supplemental Figure 13B). Since fewer DEGs were identified as VI-specific, there were few regulated pathway modules detected (Supplemental Figures 14C and D, 15C and D).

Overall, these data show that SARS-CoV-2 infection induced largely similar transcriptional programs in immune cells for both VI and MI animals, including many viral response and immune activation pathways. In MI-specific transcriptional programs, positive regulation of cytokine signaling stood out as enriched across all cell types studied, while cellular maintenance functions were typically downregulated. On the other hand, in the VI animals, the magnitude of gene expression was lower and fewer differential genes were detected, resulting in few regulated pathway modules.

DISCUSSION

In humans, COVID-19 can progress to severe clinical disease which manifests as pneumonia. mRNA-1273 was previously shown to be efficacious in NHPs (8), mice (1) and recently, in a large Phase 3 trial (11). Hamsters consistently exhibit the hallmarks of severe COVID-19 disease and are therefore an important and stringent model for preclinical vaccine efficacy studies. We show that two doses of mRNA-1273 reduced viral load in the upper and lower airways of hamsters and protected against weight loss, while a prime-only vaccination provided partial protection. Neutralizing titers were not dependent on dosage in a prime-boost schedule, yet the highest prime-boost dose of 25 μg provided better protection against lung injury and weight loss. Despite a strong inverse correlation between neutralizing antibody titers and virus load in the respiratory tract, the inverse correlation between neutralizing or binding antibody titers and weight loss was

only moderate. Therefore, other antibody- or cell-mediated mechanisms may be required for complete protection against SARS-CoV-2 disease in this model. This emphasizes the importance of a qualitative, not just quantitative, immune response, which may be influenced by the vaccine dose and regimen. The efficacy of mRNA-1273 in hamsters is distinguished from efficacy studies with NHP and mouse models, as protection was afforded against severe pathological phenotypes and clinical disease, including high levels of virus replication, weight loss and extensive pneumonia, and immunity was more permissive to infection.

Gene expression functional pathways in vaccinated hamsters appeared to promote pulmonary homeostasis and a less proliferative and migratory response following infection while supporting virus clearance. While enriched gene expression pathways associated with immune effector functions were shared by both VI and MI hamsters, pathways regulating cell migration were generally unique to MI hamsters. Granulocytes and inflammatory macrophages were abundant in the lungs of MI hamsters, features that are also observed in patients with severe COVID-19 (31, 46). High viral RNA reads within these cells suggests acquisition of infected cells by phagocytosis or a susceptibility to infection. Vaccination averted pro-inflammatory responses and the influx of these innate immune cells. The dominant CCL8 response across all immune cells in MI hamsters was restricted to macrophages in VI hamsters and may represent a signal for regulated cellular trafficking as opposed to inflammation. Similar levels of monocytes infiltrated the lungs of both MI and VI hamsters. While monocytes from both MI and VI hamsters possessed DEGs compared to N samples that modulated their responses to external stimulus, the monocytes from MI, but not VI, hamsters exhibited upregulated inflammatory characteristics that are observed in severe COVID-19 cases (47). The controlled responses in VI monocytes suggest a supportive role in immune regulation. Upregulated adaptation to oxidative stress in monocytes, NK cells and $CD8^+$ T cells was unique to MI hamsters, indicating that vaccination controlled exacerbated responses to infection which promotes tissue damage and hypoxic respiratory failure in severe patients (48).

Certain NK cell phenotypes were associated with COVID-19 related hyperinflammation and similar to the populations in the BALF from patients with severe disease (49); the cytotoxic functions of NK cells in MI hamsters were enriched while their proliferation processes were negatively regulated. NK cells in VI hamsters were functioning in a similar albeit attenuated capacity, to those in MI hamsters, which suggests a reduced ability to clear virus-infected cells. NK cells maintained immune homeostasis in the lungs upon infection of mice vaccinated against influenza, rather than realizing their killing capacity, to enable virus clearance by the adaptive immune system with minimal pathology (50). We found that the transcriptional program to infection in lymphoid and myeloid cells is comparable but of much reduced amplitude in VI compared with MI hamsters, and the VI hamsters also show an attenuated CCL8 induction across immune cells. Overall, we interpret this as indicative of a generally lower state of innate immune cell activation in response to infection in the vaccinated hamsters. mRNA-1273 vaccination may enable a controlled cellular antiviral response conducive to preserving the lung milieu.

Patients with severe COVID-19 display aberrant T cell activation and differentiation, lymphopenia (51, 52), and generally have more proliferative T cells but less $CD8^+$ T cell proportions with limited clonal diversity in BALF (31). Conversely, non-hospitalized, recovered individuals have virus-specific T cell memory (53, 54). In the lungs of MI hamsters, T cell proportions declined indicating that extravasation to affected tissues, a suggested cause of lymphopenia in severe patients, was not occurring. Instead, $CD8^+$ T cells from MI hamsters were downregulated for pathways supportive of cell cycling and survival during activation of naïve T cells or environmental stresses, including macroautophagy and telomere maintenance (55, 56), despite their upregulation in responsiveness to oxidative stress and cytokine stimulus. Therefore, $CD8^+$ T cells in MI hamsters may develop an effector phenotype but are replicative senescent, susceptible to depletion or unable to form functional memory T cells (57, 58). $CD8^+$ T cell exhaustion from hyperactivation or augmented expression of pro-apoptotic molecules has been linked to their depletion in severe

COVID-19 cases (59, 60). Vaccination prevented a reduction in T-cell frequencies in the lungs following infection. Rather, greater proportions of dividing $CD4^+$ T cells were found in VI hamsters compared to MI hamsters which appeared to represent a Th1 polarized recall response. While $CD8^+$ T cells in VI hamsters were less enriched for activation and proliferative pathways compared to MI hamsters, they sustained effector function pathways. This suggests the $CD8^+$ T cell response in VI hamsters was either from memory effectors established after vaccination, to facilitate viral clearance, or from clonally diverse, tissue-resident cells with an effector phenotype after SARS-CoV-2 challenge, as seen in the BALF from moderate but not severe COVID-19 patients (31).

Aberrant T cell responses or their depletion in severe COVID-19 may be indirectly attributed to DCs that are impaired in maturation and T cell activation (61). DC subsets infiltrated the lungs of MI hamsters but remained unaltered in VI hamsters. Similar to acute phase coronavirus infections (62), infiltrating pDCs may provide rapid antiviral responses through the upregulation of cytokine production pathways. However, pDCs were not necessary for influenza A virus clearance and were shown to have a deleterious role on $CD8^+$ T cells during lethal infection of mice (63, 64). In MI hamsters, the lymphoid organ development pathway of pDCs was downregulated suggesting their role in T cell differentiation was compromised. The low numbers of pDCs in VI hamsters and their limited DEGs suggests they were not involved in vaccine-mediated responses to infection. Dysfunctional T cell activation in COVID-19 patients has been associated with the downregulation of MHC and costimulatory molecules on antigen presenting cells (61, 65, 66). Immune effector pathways and chemotactic cues from IL-1 to migrate to the lung-draining lymph nodes were upregulated in cDCs from both MI and VI hamsters, while DEGs involved in the activation of T cells via MHC molecules were paradoxically downregulated. Despite this remarkable similarity in MI and VI-induced cDC pathways, disparities in DEG expression magnitude, cDC numbers and external stimulus from the lung milieu may account for different cDC-mediated outcomes.

Diminished MHC-dependent T cell activation by cDCs from MI hamsters likely impaired the adaptive immune response, while in VI hamsters, the controlled cell contact dependent activation by cDCs may be sufficient for recall responses or sustaining the effector functions of $CD8^+$ T cells (67). mRNA-1273 promoted a controlled response to SARS-CoV-2 infection that prevented desynchrony between the innate and adaptive immune arms which can exacerbate inflammation and disease severity.

The incomplete annotation of the hamster genome prevented identification of highly specific subtypes within immune cell populations. In particular, we were unable to identify resident memory cells which are important for recall responses and durable immunity. Cell type identification partially based on mouse data and the pathway analysis based on human gene ontology terms did permit detailed profiling of cellular responses. While this study examined the response to infection directly in the lungs of VI and MI hamsters rather than BALF, scRNA-seq analysis was limited to the cranial lobe of the lung and responses to an infection may be spatially distinct. As a result, we captured the functional dynamics of neutrophils/heterophils within a potential focal inflammatory lesion, formed after infection of a low vaccine-dose VI hamster. This finding, along with excessive weight loss exhibited by this outlier hamster, may underscore the importance of dose in achieving complete protection against severe disease.

mRNA-1273 provided hamsters with infection-permissive immunity that following SARS-CoV-2 infection reduced virus load and severe disease by promoting humoral responses in the periphery and antiviral cellular responses in the lung. mRNA-1273 demonstrated protection is predominately achieved through the induction of antibodies, and cellular responses may act to support complete clearance of the virus. Importantly, the safety of mRNA-1273 was indicated by the absence of aberrant cellular pathways in VI hamsters after challenge. Transient, low level virus replication in VI hamsters did trigger the regulation of cellular programs in some immune cells that were strikingly similar to MI hamsters. However, the responses were attenuated and lacked the atypical

manifestations which contribute to inflammation and lung injury in critical COVID-19 cases. The surprising commonalities in transcriptional pathway regulation between vaccinated and mock vaccinated recipients during acute infection warrants investigation into how immunity induced by other vaccines is regulated following infection to provide the foundation for successful vaccination.

METHODS

Pre-clinical mRNA-1273 mRNA and LNP production process

Pre-clinical mRNA-1273 is a purified mRNA transcript encoding the prefusion-stabilized SARS-CoV-2 S-2P protein and encapsulated by a lipid nanoparticle. The process for mRNA synthesis, purification, and encapsulation was described previously (1).

ELISA

S, RBD or nucleocapsid proteins (1µg/mL, Sino Biological) were coated onto 96-well plates for 16 h. Plates were then blocked with SuperBlock (Pierce). Five-fold serial dilutions of hamster serum were then added to the plates (assay diluent – PBS + 0.05% Tween-20 + 5% goat serum) and incubated for 2 hours at 37°C. Bound antibodies were detected with HRP-conjugated goat anti-hamster IgG (1:10,000 Abcam AB7146). Following the addition of TMB substrate (SeraCare #5120-0077) and TMB stop solution (SeraCare #5150-0021), the absorbance was measured at OD 450 nm. Titers were determined using a four-parameter logistic curve fit in GraphPad Prism (GraphPad Software, Inc.) and defined as the reciprocal dilution at approximately OD450nm = 1.5 (normalized to a hamster standard on each plate).

Hamster study

Three groups of 6-7 week female golden Syrian hamsters (Envigo) (*n* = 15 per group) were vaccinated with mRNA-1273 diluted to 25 µg, 5 µg and 1 µg in PBS for prime-boost vaccine regimens. An additional group (*n* = 15) was prime vaccinated only with 25 µg of mRNA-1273. A mock vaccinated control group (*n* = 15) received PBS only. Formulations were administered by IM injection to each hind leg (50 µL per dose site). At week 3, prime-boost groups received their second vaccine dose. At week 6 (day 42), all animals were infected via the intranasal route with 100 µL of 2019-nCoV/USA-WA01/2020 (GenBank: MN985325.1, courtesy World Reference Center for Emerging Viruses and Arboviruses, the University of Texas Medical Branch (UTMB)) at 10^5 PFU (approximately 50 µL per nostril). Over the course of the study, hamsters were monitored daily for clinically for weight changes. On each serial endpoint day (days 2, 4 and 14 post-challenge), lungs, nasal turbinates and serum were collected from 5 hamsters per group. All animal protocols were approved by the Institutional Animal Care and Use Committee at UTMB.

Analysis of viral load by plaque assay

The right lung and nasal turbinates were homogenized in Leibovitz L-15 medium (Thermo Fisher Scientific, Cat No. 11415064)/10% FBS/1X Antibiotic-Antimycotic (Thermo Fisher Scientific, Cat No.15240062) using the TissueLyser II bead mill (Qiagen) and 5 mm stainless steel beads (Qiagen, Cat No. 69989) and briefly centrifuged. Ten-fold serial dilutions of homogenates were prepared in serum free MEM media and absorbed on Vero-E6 monolayers in 48 well plate for 1 hour at 37°C. The virus inoculum was removed replaced with an overlay of MEM/methylcellulose/2% FBS. After 3 days, plaques were immunostained with a human monoclonal antibody cocktail specific for the S protein (Distributed Bio) and an anti-human IgG HRP conjugated secondary antibody (Sera Care Cat No.5220-0456). Plaques were counted and virus load per gram tissue was determined.

Analysis of viral load by qRT-PCR

Replicating viral RNA was determined in the lungs and nasal turbinates by measuring subgenomic SARS-CoV-2 E gene RNA by qRT-PCR using previously described primers, probe and cycle conditions (68). Briefly, RNA was extracted from lung and nasal turbinates homogenates using TRIZOL LS (Thermo Fisher Scientific) and Direct-zol RNA Microprep kit (Zymo Research). RNA (500 ng) was reverse transcribed using Superscript IV (Thermo Fisher Scientific) according to the manufacturer's recommendations. Quantitative real-time PCR was performed using the TaqMan Fast Advanced Master Mix (Thermo Fisher Scientific), and primers and a FAM-ZEN/Iowa Black FQ labeled probe sequence (IDT) on the QuantStudio 6 system (Applied Biosystems). An Ultramer DNA oligo (IDT) spanning the amplicon was used to generate standard curves to calculate the sgRNA copies per gram of tissue.

Histopathology

Lung samples were processed per a standard protocol for histological analysis. Briefly, the lower left lung lobe was fixed in 10% neutral buffered formalin, embedded in paraffin, sectioned at 5 µm and stained with Hematoxylin and Eosin (H&E) for routine histopathology. Samples were evaluated by a board-certified veterinary pathologist in a blinded manner. Sections were examined under light microscopy using an Olympus BX51 microscope and photographs were taken using an Olympus DP73 camera. Representative sections were displayed.

Single cell isolation and RNA sequencing

The cranial left lung sections taken at the time of necropsy at 4 dpi from the 5 µg prime-boost group (VI, *n* = 5), mock vaccinated group (MI, *n* = 5) and a naïve group (N, *n* = 4) of hamsters

that were mock infected via the IN route with 100 µL of media inoculum. Lung samples were enzymatically digested and homogenized using the Lung Dissociation kit, mouse (Miltenyi Biotec Cat No. 130-095-927) and GentleMACS Dissociator (Miltenyi Biotec) according to the manufacturer's protocol. After 30 min of digestion, the samples were filtered through a 70 µM filter, and RBC lysis was performed (ThermoFisher, Cat #00-4333-57). After two washes in PBS containing 0.05 mM EDTA and 0.04% BSA, the cell pellet was re-suspended in 1ml of buffer and filtered through a 40 µM Flowmi Cell strainer (Bel-Art # H13680-0040). The cell viability and concentration were determined on a TC20 cell counter (Bio-Rad, CA). Dead cell removal was performed if the viability was lower than 80% using Dead Cell Removal Kit (Miltenyi Biotec, Cat#130-090-101) as per manufacturer's recommendations.

Seven thousand cells were targeted for generation of barcoded gel bead emulsions using the Chromium Single Cell 3' version 3.0 chemistry (10x Genomics, Cat# 1000077). After reverse transcription, the cDNA was amplified and purified using SPRISelect magnetic beads (Beckman Coulter, CA, Cat#B23317). The purified cDNA was precipitated in 80% ethanol, removed from BSL-4 containment, tested for quality on Bioanalyzer, and 3' gene expression libraries were prepared as per manufacturer's instructions. Libraries were quantified, and pooled libraries were submitted for sequencing (~140,000 reads per sample) on Novaseq S1 Flow cell (New York Genome Center).

Processing of scRNA-seq data

scRNA-seq data were processed using the Cell Ranger pipeline (v4.0.0). Alignment was done against the Mesocricetus auratus Ensembl genome (MesAur1.0). STARsolo was used to quantify reads associated with the viral genome by aligning against the SARS-CoV-2 genome (ASM985889v3). The 5' leader sequence and 3' UTR of the SARS-CoV-2 genome were included as reference gtf entries. Resulting count tables were then analyzed using Seurat (V3.1.5) (69).

Cells with abnormally high mitochondrial gene content (greater than 20% of UMIs per cell) and/or cells containing less than 300 unique genes were removed. A single sample in the VI group was a clear outlier (see Supplemental Figure 8) and was removed from all further analysis. For each group (MI: *n* = 5, VI: *n* = 4, and N: *n* = 4), all samples were merged in an unbiased manner. The three resulting datasets (one per group) were then integrated using the "IntegrateData()" function of Seurat, to account for potential batch effects. Finally, the PCA and UMAP (70) projections were calculated for the integrated sample set using the top 2000 highly variable genes, as determined by Seurat, and significant cell clusters were identified.

Cell type identification for scRNA-seq data

Integration of the data from 13 samples comprising 50,694 cells identified 17 cell types. Single-cell Mouse Cell Atlas (scMCA) (71) was used to guide cell type identification. Reference gene markers were initially determined from the MCA adult lung dataset. For each cell-type, marker genes were defined as genes satisfying two conditions. Then, the average logFC of each marker gene was greater than 1.0 as compared to the other cell types. Second, the fraction of cells expressing the marker gene in the cell type was higher than the fraction of cells expressing the marker gene in all other cell types by at least 0.4. Using the defined marker gene lists, the correlation of the average gene expression in each cell type in the MCA adult lung was computed with each cell in our dataset, annotating each cell with the most highly correlated cell type. Additional marker sets and prior knowledge (72) was used for some cell-types that were ambiguous or missing from the reference data (granulocytes, activated $CD8^+$T cells, dendritic cell subtypes). Cell subtypes in some instances were aggregated (pneumocytes, bronchiolar epithelial cells, dendritic cell subtype). Activated $CD8^+$ T cells were identified by the co-expression of $CD8^+$ T cell markers and NK cell markers, along with too low read count to be considered

doublets. To identify clusters consisting of cells undergoing rapid cell division, scMCA's labeling of dividing cells was used. These clusters were combined into a single population named "Dividing Immune Cells", as cells within this population expressed markers for both lymphocytes and myeloid cells. This cluster annotation was also corroborated with the CellCycleScoring() function in Seurat, where 97.7% of the cells in the dividing immune cell cluster were predicted to be in G2M (59.4%) or S (38.3%) phase. To account for invading cell types that were only present in MI samples, the interstitial macrophage and alveolar macrophage cells were removed from the cell type proportion calculations of the remaining cell types.

Cell type-specific comparisons of MI to N and VI to N

DEGs were identified in scRNA-seq data for MI and VI comparisons to N in $CD8^+$ T cells, NK cells, monocytes and DC subtypes (pDCs and cDCs), using the non-parametric Wilcoxon rank sum test. The groups of DCα cells were incorporated into cDCs during DEG identification. Differential expression p-values were adjusted for multiple hypothesis testing using the Benjamini-Hochberg procedure (45). DEGs with FDR < 0.05 and absolute logFC > 0.1 for each comparison were selected as significant. To study gene function and pathway enrichment among DEGs, golden hamster genes were mapped to homolog genes in the homo sapiens species using Biomart (http://www.ensembl.org/biomart). Selected genes were used to construct a functional network built by HumanBase (https://hb.flatironinstitute.org) specifically of the lung tissue (45). Neighboring genes that form a community are clustered into functional modules using the graph-based Louvain clustering algorithm based on the network-predicted functional similarity between genes in the lung tissue. Gene ontology term enrichment was performed for genes in each module, while the direction of regulation for enriched pathways is elicited using a z-score, which is defined as $z = \frac{N_{up} - N_{down}}{N_{up} + N_{down}}$, where N_{up} represents the number of up-regulated DEGs (positive

logFC) in that module and N_{down} represents the number of down-regulated DEGs (negative logFC). Significantly enriched terms with adjusted p-value (q-value) < 0.05 were selected. Each module was annotated with distinct and representative gene ontology terms. For $CD8^+$ T cells, NK cells, cDCs and monocytes, gene functional clustering and enrichment analysis was performed for DEGs that were common to the MI and VI comparisons to N (Figure 6A and B and Figure 7A and B) and DEGs that are specific to either the MI or VI comparisons to N only (Supplemental Figure 14 and Supplemental Figure 15). For pDCs, however, functional clustering and enrichment analysis was only performed on MI vs. N given the insufficient number of DEGs in VI vs. N (Supplemental Figure 13B).

Statistical analysis

Statistical analysis was performed using GraphPad Prism software, version 6. Two-way ANOVA with Tukey's or Sidak's corrections were respectively performed for multiple comparisons between vaccine groups or between time points. Significance between pre- and post- infection antibody titers was measured by multiple t tests with Holm Sidak's correction for multiple comparisons (Supplemental Figure 4). ANOVA and post-hoc Tukey's test pairwise comparisons were employed to determine the significance of scRNA-seq-based cell type proportion changes (Figure 3, Supplemental Figure 7B). Correlations were determined by two-sided Spearman's rank tests. $*P < 0.05$, $**P < 0.01$, $***P < 0.001$, $****P < 0.0001$. For lymphocyte marker comparisons (Supplemental Figures 11, 12D), markers were selected for known functional activity, and exhibiting both a statistically significant change ($P < 0.05$) and expression in at least 10% of the cells in a cell type.

Data availability

RNA sequencing data have been deposited in NCBI's Gene Expression Omnibus and are accessible through the GEO Series accession number GSE163838.

REFERENCES

1. Corbett KS, Edwards DK, Leist SR, Abiona OM, Boyoglu-Barnum S, Gillespie RA, Himansu S, Schafer A, Ziwawo CT, DiPiazza AT, et al. SARS-CoV-2 mRNA vaccine design enabled by prototype pathogen preparedness. *Nature.* 2020.
2. Meyer M, Huang E, Yuzhakov O, Ramanathan P, Ciaramella G, and Bukreyev A. Modified mRNA-Based Vaccines Elicit Robust Immune Responses and Protect Guinea Pigs From Ebola Virus Disease. *J Infect Dis.* 2018;217(3):451-5.
3. Feldman RA, Fuhr R, Smolenov I, Mick Ribeiro A, Panther L, Watson M, Senn JJ, Smith M, Almarsson, Pujar HS, et al. mRNA vaccines against H10N8 and H7N9 influenza viruses of pandemic potential are immunogenic and well tolerated in healthy adults in phase 1 randomized clinical trials. *Vaccine.* 2019;37(25):3326-34.
4. Aliprantis AO, Shaw CA, Griffin P, Farinola N, Railkar RA, Cao X, Liu W, Sachs JR, Swenson CJ, Lee H, et al. A phase 1, randomized, placebo-controlled study to evaluate the safety and immunogenicity of an mRNA-based RSV prefusion F protein vaccine in healthy younger and older adults. *Hum Vaccin Immunother.* 2020:1-14.
5. ClinicalTrials.gov. A Phase 1, Randomized, Observer-Blind, Placebo-Controlled, Dose-Ranging Study to Evaluate the Safety, Reactogenicity, and Immunogenicity of Cytomegalovirus Vaccines mRNA-1647 and mRNA-1443 When Administered to Healthy Adults. https://clinicaltrials.gov/ct2/show/NCT03382405.
6. ClinicalTrials.gov. A Phase 1, Randomized, Observer-Blind, Placebo-Controlled, Dose-Ranging Study to Evaluate the Safety, Reactogenicity, and Immunogenicity of mRNA-

1653, a Combined Human Metapneumovirus and Human Parainfluenza Virus Type 3 Vaccine, When Administered to Healthy Adults. https://clinicaltrials.gov/ct2/show/NCT03392389.

7. ClinicalTrials.gov. A Phase 1, Randomized, Observer-Blind, Placebo-Controlled, Dose-Ranging Study to Evaluate the Safety, Tolerability, and Immunogenicity of Zika Vaccine mRNA-1893 in Healthy Flavivirus Seropositive and Seronegative Adults. https://clinicaltrials.gov/ct2/show/NCT04064905.
8. Corbett KS, Flynn B, Foulds KE, Francica JR, Boyoglu-Barnum S, Werner AP, Flach B, O'Connell S, Bock KW, Minai M, et al. Evaluation of the mRNA-1273 Vaccine against SARS-CoV-2 in Nonhuman Primates. *N Engl J Med.* 2020.
9. Jackson LA, Anderson EJ, Rouphael NG, Roberts PC, Makhene M, Coler RN, McCullough MP, Chappell JD, Denison MR, Stevens LJ, et al. An mRNA Vaccine against SARS-CoV-2 - Preliminary Report. *N Engl J Med.* 2020.
10. Anderson EJ, Rouphael NG, Widge AT, Jackson LA, Roberts PC, Makhene M, Chappell JD, Denison MR, Stevens LJ, Pruijssers AJ, et al. Safety and Immunogenicity of SARS-CoV-2 mRNA-1273 Vaccine in Older Adults. *N Engl J Med.* 2020.
11. Baden LR, El Sahly HM, Essink B, Kotloff K, Frey S, Novak R, Diemert D, Spector SA, Rouphael N, Creech CB, et al. Efficacy and Safety of the mRNA-1273 SARS-CoV-2 Vaccine. *N Engl J Med.* 2020.
12. Munster VJ, Feldmann F, Williamson BN, van Doremalen N, Perez-Perez L, Schulz J, Meade-White K, Okumura A, Callison J, Brumbaugh B, et al. Respiratory disease in rhesus macaques inoculated with SARS-CoV-2. *Nature.* 2020;585(7824):268-72.
13. Rockx B, Kuiken T, Herfst S, Bestebroer T, Lamers MM, Oude Munnink BB, de Meulder D, van Amerongen G, van den Brand J, Okba NMA, et al. Comparative pathogenesis of COVID-19, MERS, and SARS in a nonhuman primate model. *Science.* 2020;368(6494):1012-5.

14. Woolsey C, Borisevich V, Prasad AN, Agans KN, Deer DJ, Dobias NS, Heymann JC, Foster SL, Levine CB, Medina L, et al. Establishment of an African green monkey model for COVID-19 and protection against re-infection. *Nat Immunol.* 2021;22(1):86-98.

15. Shi J, Wen Z, Zhong G, Yang H, Wang C, Huang B, Liu R, He X, Shuai L, Sun Z, et al. Susceptibility of ferrets, cats, dogs, and other domesticated animals to SARS-coronavirus 2. *Science.* 2020;368(6494):1016-20.

16. Kim YI, Kim SG, Kim SM, Kim EH, Park SJ, Yu KM, Chang JH, Kim EJ, Lee S, Casel MAB, et al. Infection and Rapid Transmission of SARS-CoV-2 in Ferrets. *Cell Host Microbe.* 2020;27(5):704-9 e2.

17. Blanco-Melo D, Nilsson-Payant BE, Liu WC, Uhl S, Hoagland D, Moller R, Jordan TX, Oishi K, Panis M, Sachs D, et al. Imbalanced Host Response to SARS-CoV-2 Drives Development of COVID-19. *Cell.* 2020;181(5):1036-45 e9.

18. Dinnon KH, 3rd, Leist SR, Schafer A, Edwards CE, Martinez DR, Montgomery SA, West A, Yount BL, Jr., Hou YJ, Adams LE, et al. A mouse-adapted model of SARS-CoV-2 to test COVID-19 countermeasures. *Nature.* 2020.

19. Imai M, Iwatsuki-Horimoto K, Hatta M, Loeber S, Halfmann PJ, Nakajima N, Watanabe T, Ujie M, Takahashi K, Ito M, et al. Syrian hamsters as a small animal model for SARS-CoV-2 infection and countermeasure development. *Proc Natl Acad Sci U S A.* 2020;117(28):16587-95.

20. Chan JF, Zhang AJ, Yuan S, Poon VK, Chan CC, Lee AC, Chan WM, Fan Z, Tsoi HW, Wen L, et al. Simulation of the clinical and pathological manifestations of Coronavirus Disease 2019 (COVID-19) in golden Syrian hamster model: implications for disease pathogenesis and transmissibility. *Clin Infect Dis.* 2020.

21. Tostanoski LH, Wegmann F, Martinot AJ, Loos C, McMahan K, Mercado NB, Yu J, Chan CN, Bondoc S, Starke CE, et al. Ad26 vaccine protects against SARS-CoV-2 severe clinical disease in hamsters. *Nat Med.* 2020.

22. Sia SF, Yan LM, Chin AWH, Fung K, Choy KT, Wong AYL, Kaewpreedee P, Perera R, Poon LLM, Nicholls JM, et al. Pathogenesis and transmission of SARS-CoV-2 in golden hamsters. *Nature.* 2020;583(7818):834-8.

23. Winkler ES, Bailey AL, Kafai NM, Nair S, McCune BT, Yu J, Fox JM, Chen RE, Earnest JT, Keeler SP, et al. SARS-CoV-2 infection of human ACE2-transgenic mice causes severe lung inflammation and impaired function. *Nat Immunol.* 2020.

24. Wood DE, Lu J, and Langmead B. Improved metagenomic analysis with Kraken 2. *Genome Biol.* 2019;20(1):257.

25. Butler A, Hoffman P, Smibert P, Papalexi E, and Satija R. Integrating single-cell transcriptomic data across different conditions, technologies, and species. *Nat Biotechnol.* 2018;36(5):411-20.

26. Liu T, Jia P, Fang B, and Zhao Z. Differential Expression of Viral Transcripts From Single-Cell RNA Sequencing of Moderate and Severe COVID-19 Patients and Its Implications for Case Severity. *Frontiers in Microbiology.* 2020;11(2568).

27. Pontelli MC, Castro IA, Martins RB, Veras FP, Serra LL, Nascimento DC, Cardoso RS, Rosales R, Lima TM, Souza JP, et al. Infection of human lymphomononuclear cells by SARS-CoV-2. *bioRxiv.* 2020:2020.07.28.225912.

28. Ramos da Silva S, Ju E, Meng W, Paniz Mondolfi AE, Dacic S, Green A, Bryce C, Grimes Z, Fowkes M, Sordillo EM, et al. Broad SARS-CoV-2 cell tropism and immunopathology in lung tissues from fatal COVID-19. *J Infect Dis.* 2021.

29. Liu T, Jia P, Fang B, and Zhao Z. Differential Expression of Viral Transcripts From Single-Cell RNA Sequencing of Moderate and Severe COVID-19 Patients and Its Implications for Case Severity. *Front Microbiol.* 2020;11(603509.

30. Speranza E, Williamson BN, Feldmann F, Sturdevant GL, Perez-Perez L, Meade-White K, Smith BJ, Lovaglio J, Martens C, Munster VJ, et al. Single-cell RNA sequencing

reveals SARS-CoV-2 infection dynamics in lungs of African green monkeys. *Sci Transl Med.* 2021;13(578).

31. Liao M, Liu Y, Yuan J, Wen Y, Xu G, Zhao J, Cheng L, Li J, Wang X, Wang F, et al. Single-cell landscape of bronchoalveolar immune cells in patients with COVID-19. *Nat Med.* 2020;26(6):842-4.

32. Cano-Gamez E, Soskic B, Roumeliotis TI, So E, Smyth DJ, Baldrighi M, Wille D, Nakic N, Esparza-Gordillo J, Larminie CGC, et al. Single-cell transcriptomics identifies an effectorness gradient shaping the response of CD4(+) T cells to cytokines. *Nat Commun.* 2020;11(1):1801.

33. Szabo PA, Levitin HM, Miron M, Snyder ME, Senda T, Yuan J, Cheng YL, Bush EC, Dogra P, Thapa P, et al. Single-cell transcriptomics of human T cells reveals tissue and activation signatures in health and disease. *Nat Commun.* 2019;10(1):4706.

34. Tibbitt CA, Stark JM, Martens L, Ma J, Mold JE, Deswarte K, Oliynyk G, Feng X, Lambrecht BN, De Bleser P, et al. Single-Cell RNA Sequencing of the T Helper Cell Response to House Dust Mites Defines a Distinct Gene Expression Signature in Airway Th2 Cells. *Immunity.* 2019;51(1):169-84 e5.

35. Koroleva EP, Fu YX, and Tumanov AV. Lymphotoxin in physiology of lymphoid tissues - Implication for antiviral defense. *Cytokine.* 2018;101(39-47.

36. Zhou Z, Ren L, Zhang L, Zhong J, Xiao Y, Jia Z, Guo L, Yang J, Wang C, Jiang S, et al. Heightened Innate Immune Responses in the Respiratory Tract of COVID-19 Patients. *Cell Host Microbe.* 2020;27(6):883-90 e2.

37. Oja AE, Piet B, Helbig C, Stark R, van der Zwan D, Blaauwgeers H, Remmerswaal EBM, Amsen D, Jonkers RE, Moerland PD, et al. Trigger-happy resident memory CD4(+) T cells inhabit the human lungs. *Mucosal Immunol.* 2018;11(3):654-67.

38. Schoettler N, Hrusch CL, Blaine KM, Sperling AI, and Ober C. Transcriptional programming and T cell receptor repertoires distinguish human lung and lymph node memory T cells. *Commun Biol.* 2019;2(411.

39. Xiong Y, Piao W, Brinkman CC, Li L, Kulinski JM, Olivera A, Cartier A, Hla T, Hippen KL, Blazar BR, et al. CD4 T cell sphingosine 1-phosphate receptor (S1PR)1 and S1PR4 and endothelial S1PR2 regulate afferent lymphatic migration. *Sci Immunol.* 2019;4(33).

40. Kanhere A, Hertweck A, Bhatia U, Gokmen MR, Perucha E, Jackson I, Lord GM, and Jenner RG. T-bet and GATA3 orchestrate Th1 and Th2 differentiation through lineage-specific targeting of distal regulatory elements. *Nat Commun.* 2012;3(1268.

41. Yoon HS, Scharer CD, Majumder P, Davis CW, Butler R, Zinzow-Kramer W, Skountzou I, Koutsonanos DG, Ahmed R, and Boss JM. ZBTB32 is an early repressor of the CIITA and MHC class II gene expression during B cell differentiation to plasma cells. *J Immunol.* 2012;189(5):2393-403.

42. Buchan S, Manzo T, Flutter B, Rogel A, Edwards N, Zhang L, Sivakumaran S, Ghorashian S, Carpenter B, Bennett C, et al. OX40- and CD27-mediated costimulation synergizes with anti-PD-L1 blockade by forcing exhausted CD8+ T cells to exit quiescence. *J Immunol.* 2015;194(1):125-33.

43. Williams JB, Horton BL, Zheng Y, Duan Y, Powell JD, and Gajewski TF. The EGR2 targets LAG-3 and 4-1BB describe and regulate dysfunctional antigen-specific CD8+ T cells in the tumor microenvironment. *J Exp Med.* 2017;214(2):381-400.

44. Yang C, Siebert JR, Burns R, Gerbec ZJ, Bonacci B, Rymaszewski A, Rau M, Riese MJ, Rao S, Carlson KS, et al. Heterogeneity of human bone marrow and blood natural killer cells defined by single-cell transcriptome. *Nat Commun.* 2019;10(1):3931.

45. Greene CS, Krishnan A, Wong AK, Ricciotti E, Zelaya RA, Himmelstein DS, Zhang R, Hartmann BM, Zaslavsky E, Sealfon SC, et al. Understanding multicellular function and disease with human tissue-specific networks. *Nat Genet.* 2015;47(6):569-76.

46. Chua RL, Lukassen S, Trump S, Hennig BP, Wendisch D, Pott F, Debnath O, Thurmann L, Kurth F, Volker MT, et al. COVID-19 severity correlates with airway epithelium-immune cell interactions identified by single-cell analysis. *Nat Biotechnol.* 2020;38(8):970-9.

47. Zhang JY, Wang XM, Xing X, Xu Z, Zhang C, Song JW, Fan X, Xia P, Fu JL, Wang SY, et al. Single-cell landscape of immunological responses in patients with COVID-19. *Nat Immunol.* 2020;21(9):1107-18.

48. Berlin DA, Gulick RM, and Martinez FJ. Severe Covid-19. *N Engl J Med.* 2020.

49. Maucourant C, Filipovic I, Ponzetta A, Aleman S, Cornillet M, Hertwig L, Strunz B, Lentini A, Reinius B, Brownlie D, et al. Natural killer cell immunotypes related to COVID-19 disease severity. *Sci Immunol.* 2020;5(50).

50. Mooney JP, Qendro T, Keith M, Philbey AW, Groves HT, Tregoning JS, Goodier MR, and Riley EM. Natural Killer Cells Dampen the Pathogenic Features of Recall Responses to Influenza Infection. *Front Immunol.* 2020;11(135.

51. Chen G, Wu D, Guo W, Cao Y, Huang D, Wang H, Wang T, Zhang X, Chen H, Yu H, et al. Clinical and immunological features of severe and moderate coronavirus disease 2019. *J Clin Invest.* 2020;130(5):2620-9.

52. Tan L, Wang Q, Zhang D, Ding J, Huang Q, Tang YQ, Wang Q, and Miao H. Lymphopenia predicts disease severity of COVID-19: a descriptive and predictive study. *Signal Transduct Target Ther.* 2020;5(1):33.

53. Grifoni A, Weiskopf D, Ramirez SI, Mateus J, Dan JM, Moderbacher CR, Rawlings SA, Sutherland A, Premkumar L, Jadi RS, et al. Targets of T Cell Responses to SARS-CoV-2 Coronavirus in Humans with COVID-19 Disease and Unexposed Individuals. *Cell.* 2020;181(7):1489-501 e15.

54. Braun J, Loyal L, Frentsch M, Wendisch D, Georg P, Kurth F, Hippenstiel S, Dingeldey M, Kruse B, Fauchere F, et al. SARS-CoV-2-reactive T cells in healthy donors and patients with COVID-19. *Nature.* 2020.

55. Lum JJ, DeBerardinis RJ, and Thompson CB. Autophagy in metazoans: cell survival in the land of plenty. *Nat Rev Mol Cell Biol.* 2005;6(6):439-48.

56. Pua HH, Guo J, Komatsu M, and He YW. Autophagy is essential for mitochondrial clearance in mature T lymphocytes. *J Immunol.* 2009;182(7):4046-55.

57. Xu X, Araki K, Li S, Han JH, Ye L, Tan WG, Konieczny BT, Bruinsma MW, Martinez J, Pearce EL, et al. Autophagy is essential for effector CD8(+) T cell survival and memory formation. *Nat Immunol.* 2014;15(12):1152-61.

58. Akbar AN, and Vukmanovic-Stejic M. Telomerase in T lymphocytes: use it and lose it? *J Immunol.* 2007;178(11):6689-94.

59. Mathew D, Giles JR, Baxter AE, Oldridge DA, Greenplate AR, Wu JE, Alanio C, Kuri-Cervantes L, Pampena MB, D'Andrea K, et al. Deep immune profiling of COVID-19 patients reveals distinct immunotypes with therapeutic implications. *Science.* 2020;369(6508).

60. Laing AG, Lorenc A, Del Molino Del Barrio I, Das A, Fish M, Monin L, Munoz-Ruiz M, McKenzie DR, Hayday TS, Francos-Quijorna I, et al. A dynamic COVID-19 immune signature includes associations with poor prognosis. *Nat Med.* 2020;26(10):1623-35.

61. Zhou R, To KK, Wong YC, Liu L, Zhou B, Li X, Huang H, Mo Y, Luk TY, Lau TT, et al. Acute SARS-CoV-2 Infection Impairs Dendritic Cell and T Cell Responses. *Immunity.* 2020;53(4):864-77 e5.

62. Cervantes-Barragan L, Zust R, Weber F, Spiegel M, Lang KS, Akira S, Thiel V, and Ludewig B. Control of coronavirus infection through plasmacytoid dendritic-cell-derived type I interferon. *Blood.* 2007;109(3):1131-7.

63. Langlois RA, and Legge KL. Plasmacytoid dendritic cells enhance mortality during lethal influenza infections by eliminating virus-specific CD8 T cells. *J Immunol.* 2010;184(8):4440-6.

64. Wolf AI, Buehler D, Hensley SE, Cavanagh LL, Wherry EJ, Kastner P, Chan S, and Weninger W. Plasmacytoid dendritic cells are dispensable during primary influenza virus infection. *J Immunol.* 2009;182(2):871-9.

65. Unterman A, Sumida TS, Nouri N, Yan X, Zhao AY, Gasque V, Schupp JC, Asashima H, Liu Y, Cosme C, et al. Single-Cell Omics Reveals Dyssynchrony of the Innate and Adaptive Immune System in Progressive COVID-19. *medRxiv.* 2020:2020.07.16.20153437.

66. Wilk AJ, Rustagi A, Zhao NQ, Roque J, Martinez-Colon GJ, McKechnie JL, Ivison GT, Ranganath T, Vergara R, Hollis T, et al. A single-cell atlas of the peripheral immune response in patients with severe COVID-19. *Nat Med.* 2020;26(7):1070-6.

67. McGill J, Van Rooijen N, and Legge KL. IL-15 trans-presentation by pulmonary dendritic cells promotes effector CD8 T cell survival during influenza virus infection. *J Exp Med.* 2010;207(3):521-34.

68. Wolfel R, Corman VM, Guggemos W, Seilmaier M, Zange S, Muller MA, Niemeyer D, Jones TC, Vollmar P, Rothe C, et al. Virological assessment of hospitalized patients with COVID-2019. *Nature.* 2020;581(7809):465-9.

69. Stuart T, Butler A, Hoffman P, Hafemeister C, Papalexi E, Mauck WM, 3rd, Hao Y, Stoeckius M, Smibert P, and Satija R. Comprehensive Integration of Single-Cell Data. *Cell.* 2019;177(7):1888-902 e21.

70. Becht E, McInnes L, Healy J, Dutertre CA, Kwok IWH, Ng LG, Ginhoux F, and Newell EW. Dimensionality reduction for visualizing single-cell data using UMAP. *Nat Biotechnol.* 2018.

71. Sun H, Zhou Y, Fei L, Chen H, and Guo G. scMCA: A Tool to Define Mouse Cell Types Based on Single-Cell Digital Expression. *Methods Mol Biol.* 2019;1935(91-6.

72. Zilionis R, Engblom C, Pfirschke C, Savova V, Zemmour D, Saatcioglu HD, Krishnan I, Maroni G, Meyerovitz CV, Kerwin CM, et al. Single-Cell Transcriptomics of Human and Mouse Lung Cancers Reveals Conserved Myeloid Populations across Individuals and Species. *Immunity.* 2019;50(5):1317-34 e10.

CONTRIBUTIONS

M.M., D.E., A.C. and A.B. conceived and designed the study.

G.S-J. co-designed the vaccine construct.

C.E.M. performed the SARS-CoV-2 challenge experiment and animal procedures.

M.M. and C.P. processed hamster samples.

C.H., A.W. and L.M. performed ELISAs.

M.M. performed and analyzed SARS-CoV-2-based virology and serology assays.

P.R. performed single-cell RNA sequencing.

Y.W., G.R.S., A.B.R., X.C., Y.G. and W.C. analyzed single-cell RNA sequencing data.

K.W.B., M. Minai and B.M.N. performed histopathology and immunohistochemistry.

I.N.M. and S.P. analyzed the histopathology data.

I.N.M. analyzed the immunohistochemistry data.

P-Y.S. contributed a new reagent.

M.M., Y.W., G.R.S., A.B.R., X.C. and I.N.M. prepared manuscript figures and tables.

M.M., Y.W., G.R.S., A.B.R., X.C., W.C., I.N.M., I.R., O.G.T., E.Z., S.C.S. and A.B. wrote the manuscript.

D.E., E.Z., O.G.T., A.C., S.C.S. and A.B. supervised the research.

All authors reviewed, edited, and approved the final version of the manuscript.

COMPETING INTERESTS

D.E., C.H., A.W., L.M, G.S-J. and A.C. are employees of Moderna, Inc. The other authors declare

no competing interests.

ACKNOWLEDGEMENTS

We thank members of the UTMB Animal Resource Center for technical assistance with the hamster experiment in ABSL-2 and ABSL-4 and husbandry support. We thank Steve Widen and the UTMB Next Generation Sequencing Core for quantification and pooling of scRNA-seq libraries for submission to the New York Genome Center. We thank the Anatomic Pathology Core facility at UTMB for embedding, sectioning and staining lung tissues for histopathology. The challenge virus used in this publication was generously provided by World Reference Center for Emerging Viruses and Arboviruses at UTMB. This work was supported by Moderna, Inc.

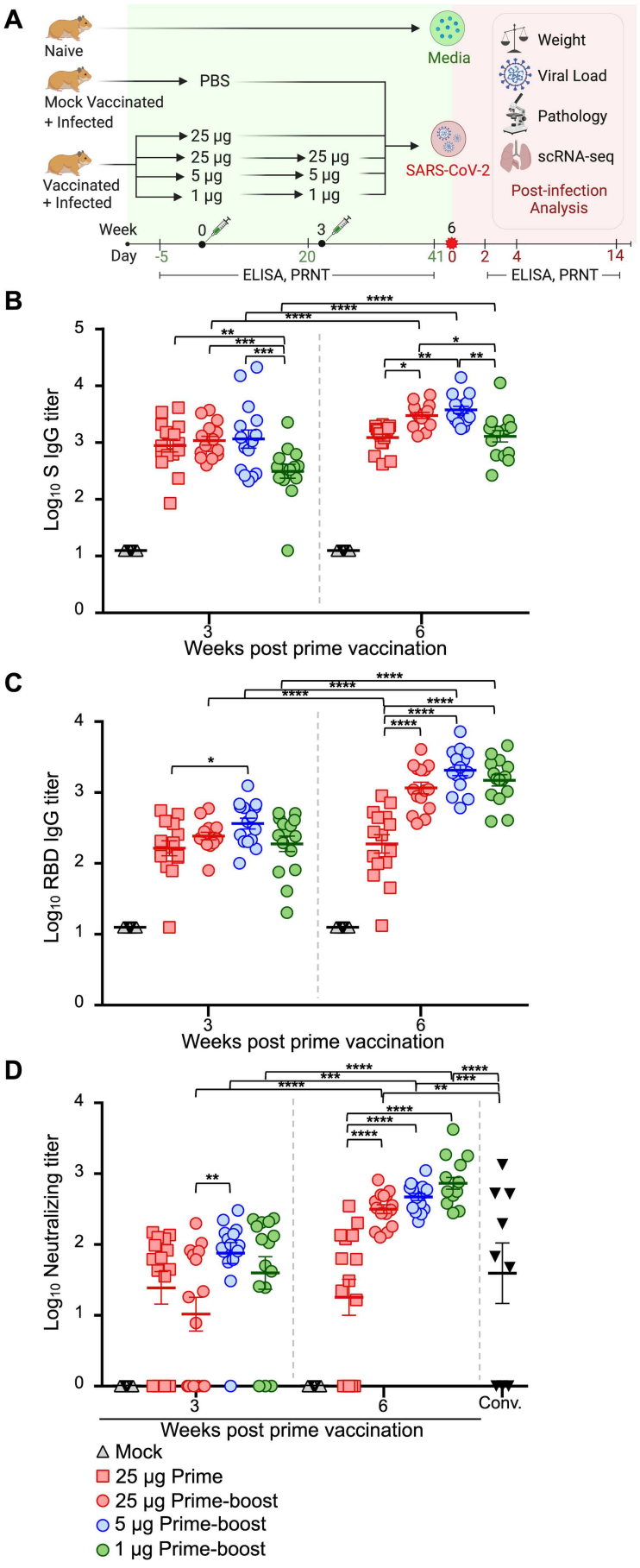
A
Naive
Media
Mock Vaccinated
+ Infected
PBS
Vaccinated
+ Infected
25 µg
25 µg
5 µg
1 µg
25 µg
5 µg
1 µg
SARS-CoV-2
Weight
Viral Load
Pathology
scRNA-seq
Post-infection
Analysis
Week
Day
0
3
6
-5
20
41
0
2
4
14
ELISA, PRNT
ELISA, PRNT
B
Log10 S IgG titer
Weeks post prime vaccination
C
Log10 RBD IgG titer
Weeks post prime vaccination
D
Log10 Neutralizing titer
Conv.
Weeks post prime vaccination
Mock
25 µg Prime
25 µg Prime-boost
5 µg Prime-boost
1 µg Prime-boost

Figure 1. Serum antibody responses in vaccinated hamsters. (A) Study design. Hamsters were prime vaccinated via the IM route at week 0 and boosted at week 3, with 25 μg (n=15), 5 μg (n=15) and 1 μg (n=15) of mRNA-1273. A group of hamsters (n=15) received a prime dose only of 25 μg mRNA-1273 and a mock group received PBS (n=15) at week 0. At week 6, animals were IN challenged with 10^5 PFU of SARS-CoV-2. On days 2, 4 and 14 post infection, hamsters (n=5 per group) were euthanized for tissue collection. Total serum SARS-CoV-2 S- (B) and RBD-specific (C) IgG titers in serum and (D) neutralizing titers in hamster groups prior to SARS-CoV-2 infection measured by ELISA and plaque reduction assays, respectively. Neutralizing titers were compared to a panel of human convalescent serum samples (Conv.). Bars denote group means ± SE. Significance measured by ANOVA with (B-D) Tukey's or Sidak's correction for multiple comparisons between vaccine groups or between time points, respectively (*P ≤ 0.05, **P ≤ 0.01, ***P ≤ 0.001, ****P ≤ 0.0001).

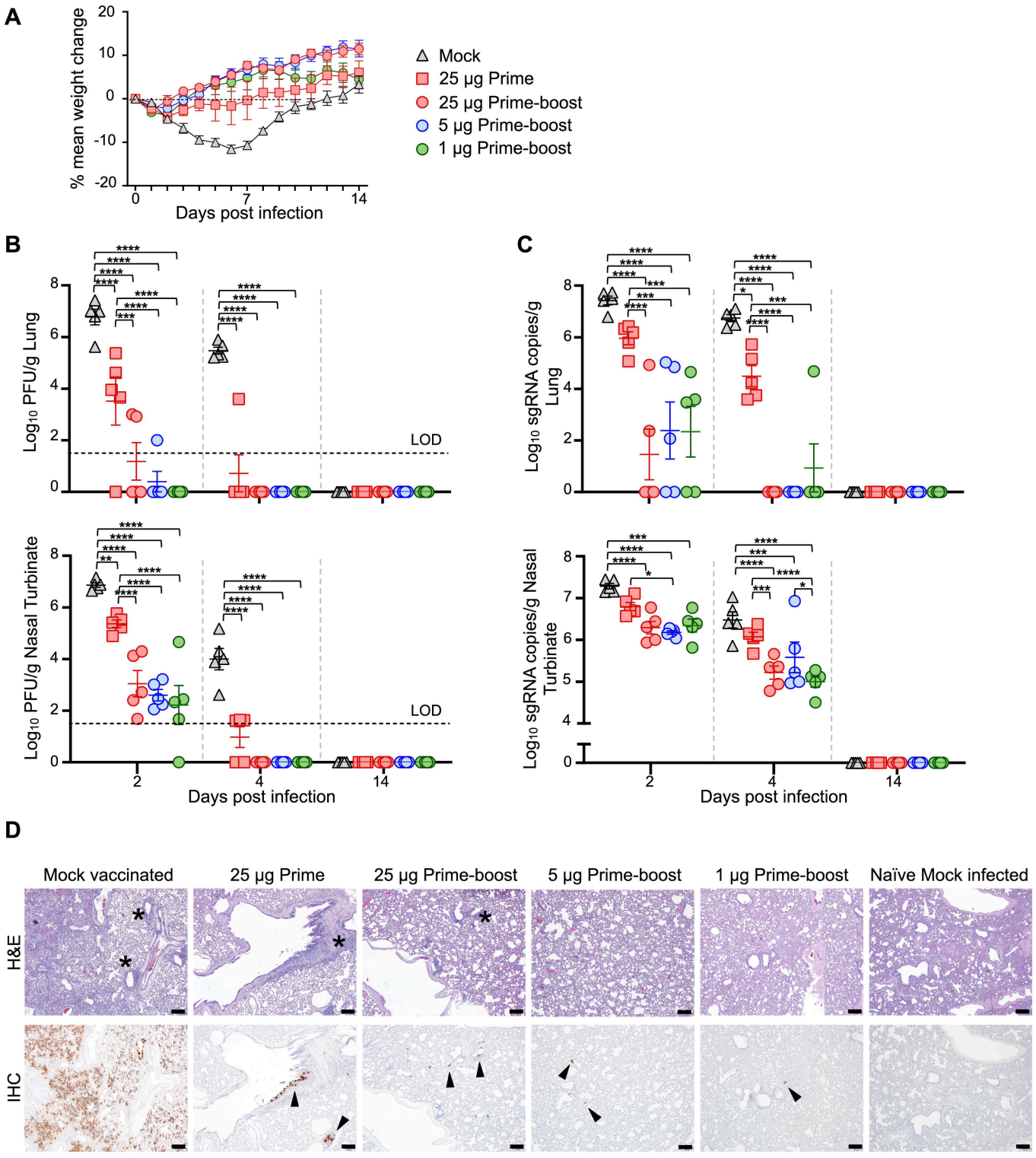
A
% mean weight change
Days post infection
Mock
25 µg Prime
25 µg Prime-boost
5 µg Prime-boost
1 µg Prime-boost
B
Log10 PFU/g Lung
Log10 PFU/g Nasal Turbinate
LOD
Days post infection
C
Log10 sgRNA copies/g Lung
Log10 sgRNA copies/g Nasal Turbinate
Days post infection
D
Mock vaccinated
25 µg Prime
25 µg Prime-boost
5 µg Prime-boost
1 µg Prime-boost
Naïve Mock infected
H&E
IHC

Figure 2. Characteristics of clinical disease following SARS-CoV-2 challenge of vaccinated hamsters. (A). Groups of 15 hamsters each vaccinated with one (25 μg) or two doses (25 μg, 5 μg and 1 μg) of mRNA-1273 or PBS were monitored for mean percent weight change over 14 days after challenge with SARS-CoV-2. (B) Viral load expressed in PFU per gram of tissue in the lungs and nasal turbinates at serial endpoint days (n=5 per group euthanized on 2, 4 and 14 dpi). Dotted line indicates limit of detection (LOD). (C) Viral sgRNA was measured by qRT-PCR in the lungs and nasal turbinates at serial endpoint days (n=5 per group euthanized on 2, 4 and 14 dpi). (B,C) Significance measured by ANOVA with Tukey's correction for multiple comparisons (*P ≤ 0.05, **P ≤ 0.01, ***P ≤ 0.001, ****P ≤ 0.0001). Error bars represent ± SE. (D) Lung sections from mock vaccinated, prime-only and prime-boost vaccinated groups infected with SARS-CoV-2 and naive mock infected groups at 4 dpi were stained with H&E, and representative photomicrographs (original magnification ×4 (scale bars, 200 μm) as indicated) from each group with virus antigen (arrowhead) in lungs, stained by IHC. * = areas of pv/pbr inflammation (mostly mononuclear).

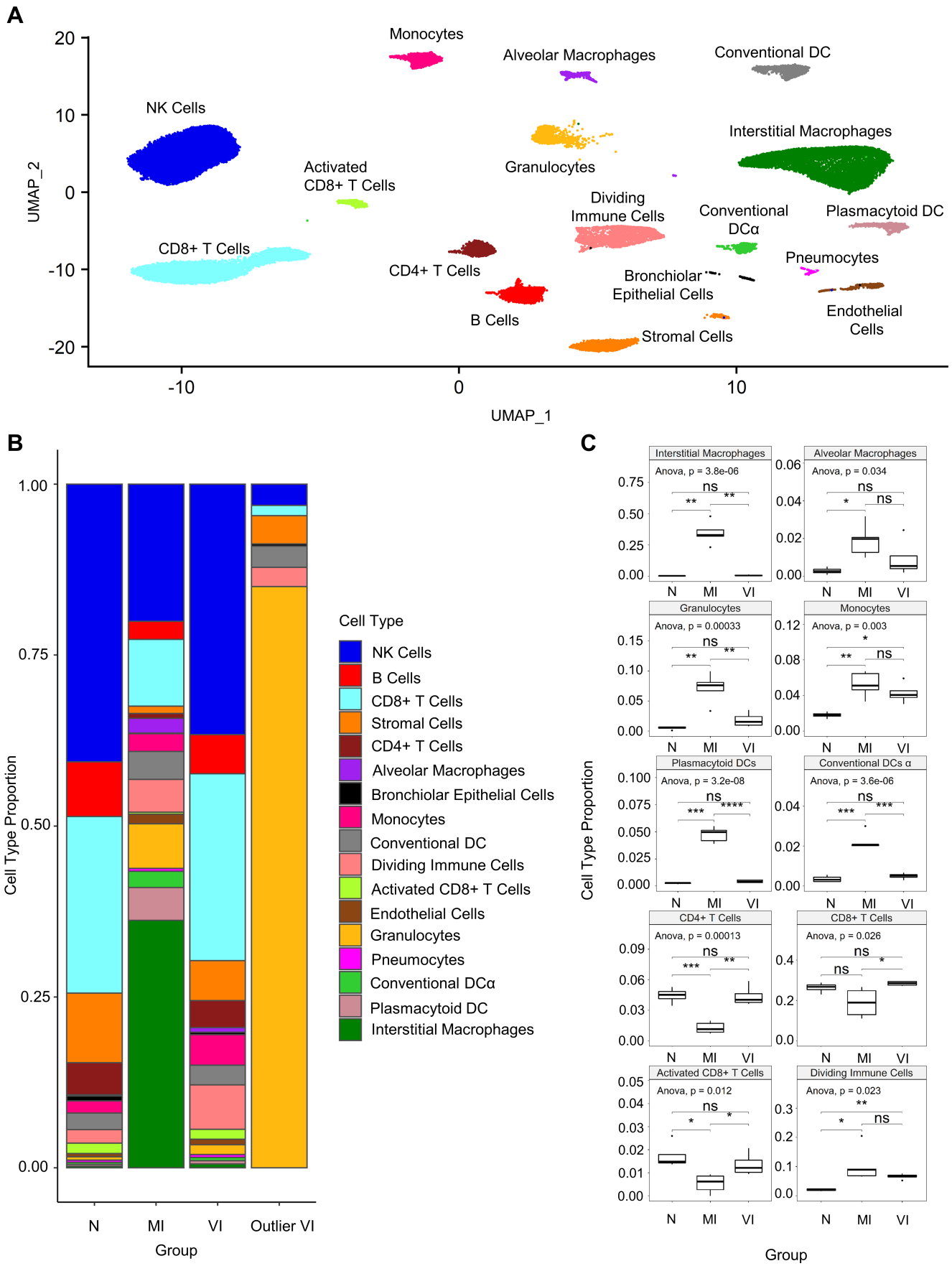
A
Monocytes
Alveolar Macrophages
Conventional DC
NK Cells
Interstitial Macrophages
Granulocytes
Activated
CD8+ T Cells
Dividing
Immune Cells
Conventional
DCα
Plasmacytoid DC
CD8+ T Cells
CD4+ T Cells
Pneumocytes
Bronchiolar
Epithelial Cells
Endothelial
Cells
B Cells
Stromal Cells
UMAP_2
UMAP_1
B
Cell Type Proportion
Group
N
MI
VI
Outlier VI
Cell Type
NK Cells
B Cells
CD8+ T Cells
Stromal Cells
CD4+ T Cells
Alveolar Macrophages
Bronchiolar Epithelial Cells
Monocytes
Conventional DC
Dividing Immune Cells
Activated CD8+ T Cells
Endothelial Cells
Granulocytes
Pneumocytes
Conventional DCα
Plasmacytoid DC
Interstitial Macrophages
C
Interstitial Macrophages
Anova, p = 3.8e-06
Alveolar Macrophages
Anova, p = 0.034
Granulocytes
Anova, p = 0.00033
Monocytes
Anova, p = 0.003
Plasmacytoid DCs
Anova, p = 3.2e-08
Conventional DCs α
Anova, p = 3.6e-06
CD4+ T Cells
Anova, p = 0.00013
CD8+ T Cells
Anova, p = 0.026
Activated CD8+ T Cells
Anova, p = 0.012
Dividing Immune Cells
Anova, p = 0.023
Cell Type Proportion
Group

Figure 3. Single-cell RNA-seq analysis of pulmonary tissues identifies cell population differences between N, MI and VI animals. (A) Integrated UMAP of all N (n=4), MI (n=5) and VI samples (n=4) excluding one VI outlier sample. (B) Bar plot of cell type proportions within N (n=4), MI (n=5), and VI (n=4) groups and VI outlier. (C) Box plots comparing cell-type proportions observed in N (n=4), MI (n=5), and VI (n=4) groups excluding one VI outlier. The limits of the box reflect the interquartile range (IQR: Q3-Q1) with median shown as horizontal bars. Whiskers extend to 1.5 times the IQR of the box. Outliers outside the 1.5*IQR are shown as individual points. ANOVA and post-hoc Tukey test pairwise comparisons are shown. * p<.05, ** p<.01, ***p<.001, **** p<.0001.

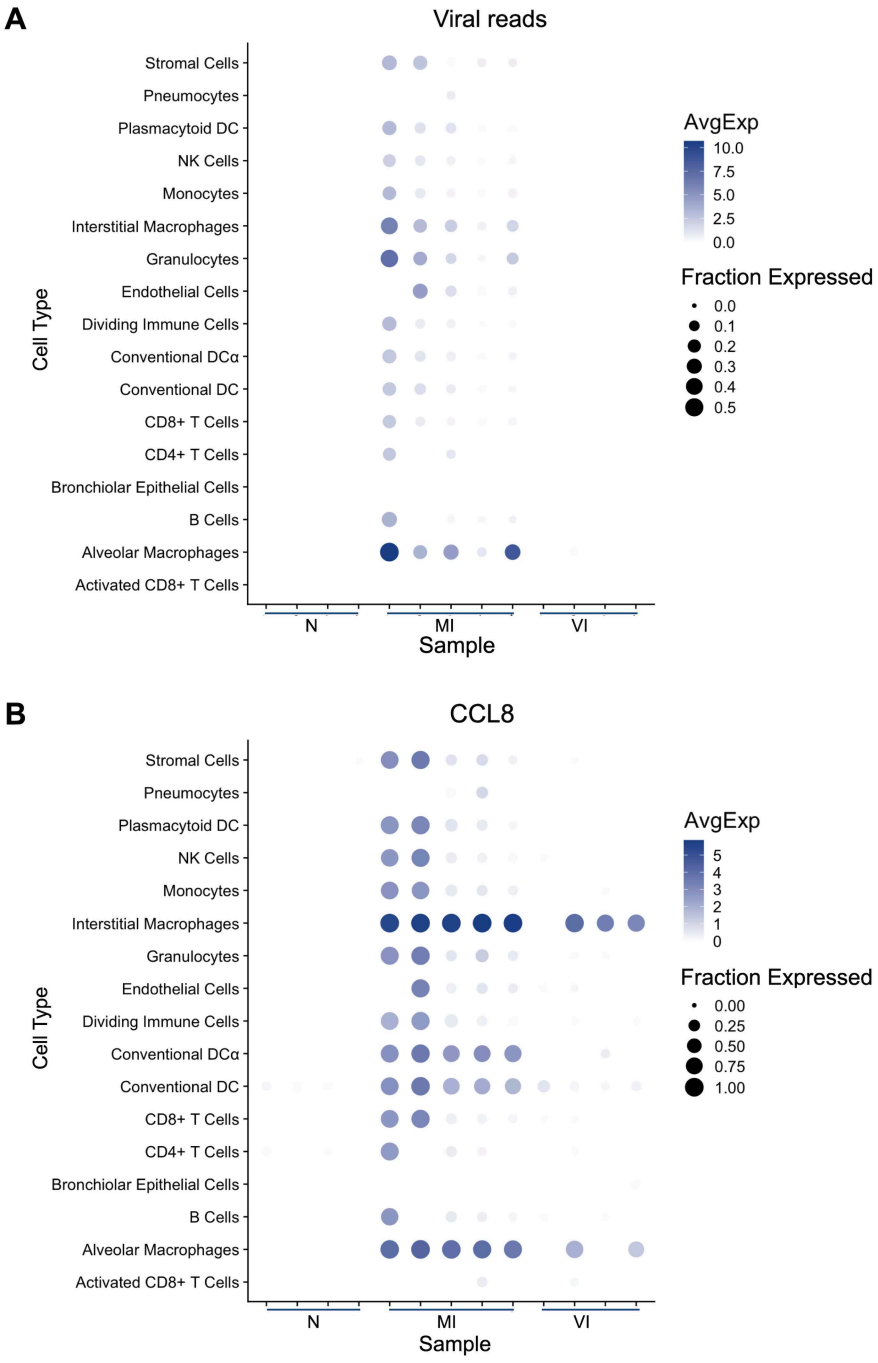
A
Viral reads
Stromal Cells
Pneumocytes
Plasmacytoid DC
NK Cells
Monocytes
Interstitial Macrophages
Granulocytes
Endothelial Cells
Dividing Immune Cells
Conventional DCα
Conventional DC
CD8+ T Cells
CD4+ T Cells
Bronchiolar Epithelial Cells
B Cells
Alveolar Macrophages
Activated CD8+ T Cells
Cell Type
N
MI
VI
Sample
AvgExp
10.0
7.5
5.0
2.5
0.0
Fraction Expressed
0.0
0.1
0.2
0.3
0.4
0.5
B
CCL8
Stromal Cells
Pneumocytes
Plasmacytoid DC
NK Cells
Monocytes
Interstitial Macrophages
Granulocytes
Endothelial Cells
Dividing Immune Cells
Conventional DCα
Conventional DC
CD8+ T Cells
CD4+ T Cells
Bronchiolar Epithelial Cells
B Cells
Alveolar Macrophages
Activated CD8+ T Cells
Cell Type
N
MI
VI
Sample
AvgExp
5
4
3
2
1
0
Fraction Expressed
0.00
0.25
0.50
0.75
1.00

Figure 4. Viral reads and CCL8 expression from lung tissue single cell RNA-seq. (A) Dot plot showing expression of all viral reads in each cell-type in N (n=4), MI (n=5) and VI (n=4) samples excluding one VI outlier sample. Cell-type/sample pairs are only shown if there are more than 20 cells per cell-type/sample. (B) Dot blot showing expression of CCL8 in each cell type in N (n=4), MI (n=5) and VI (n=4) samples excluding one VI outlier sample. Cell type/sample pairs are only shown if that are more than 20 cells per cell type/sample.

A CD8⁺ T cells

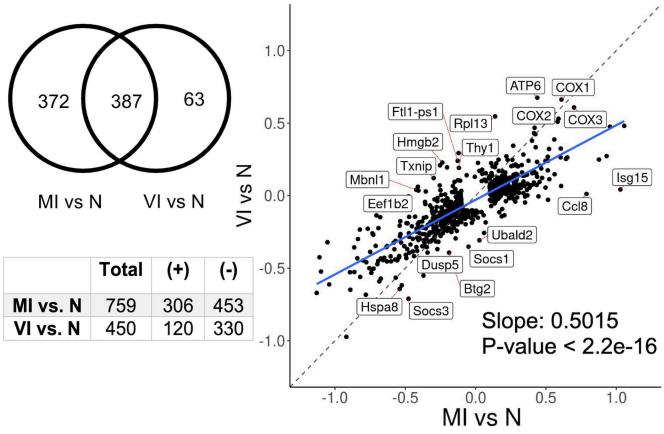

	Total	(+)	(-)
MI vs. N	759	306	453
VI vs. N	450	120	330

B NK cells

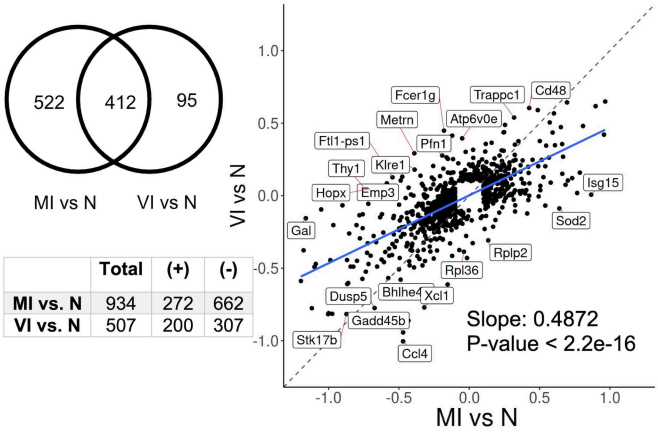

	Total	(+)	(-)
MI vs. N	934	272	662
VI vs. N	507	200	307

C Conventional DC

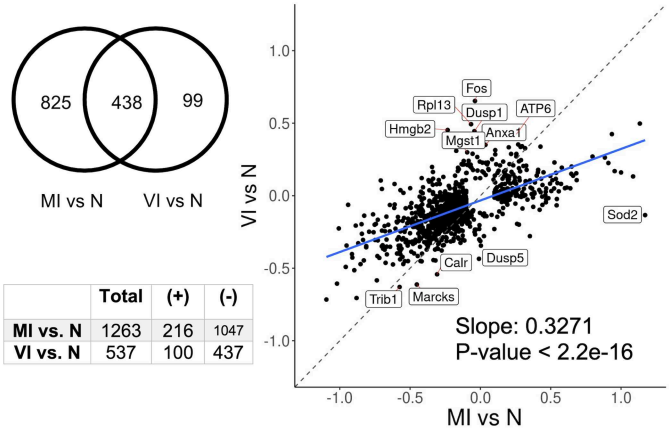

	Total	(+)	(-)
MI vs. N	1263	216	1047
VI vs. N	537	100	437

D Monocytes

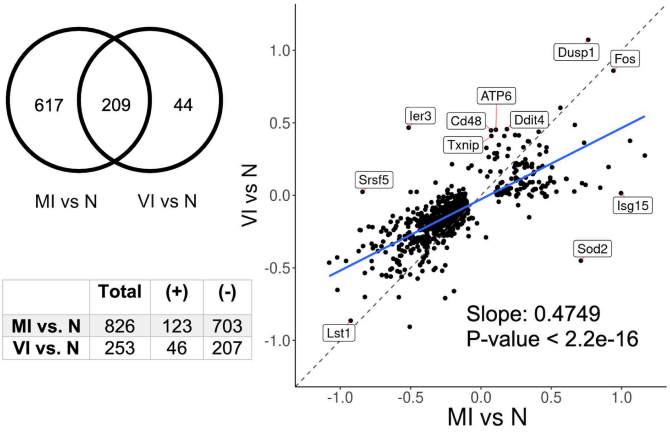

	Total	(+)	(-)
MI vs. N	826	123	703
VI vs. N	253	46	207

Figure 5. Differential gene expression analysis of MI vs. N and VI vs. N comparisons in CD8$^+$ T cells, NK cells, conventional DC (cDC), and monocytes. (A-D) Venn diagram of the union of DEGs of the two comparisons in corresponding cell types. The table below the Venn diagram indicates the total number of DEGs, number of up-regulated DEGs (positive logFC), and number of down-regulated DEGs (negative logFC) in each of the two comparisons. Scatter plot of the logFC of the union of DEGs of the two comparisons in corresponding cell types, i.e. the same group of genes as in the Venn diagram. For each comparison, DEGs were selected with thresholds FDR < 0.05 and absolute logFC > 0.1. Linear regression model was fitted to the scatter plot. Adjusted R^2 for each of the cell type is, respectively, 0.6687, 0.5147, 0.4042, and 0.5779. N: n=4; MI: n=5 and VI: n=4.

CD8⁺ T cells, common DEGs

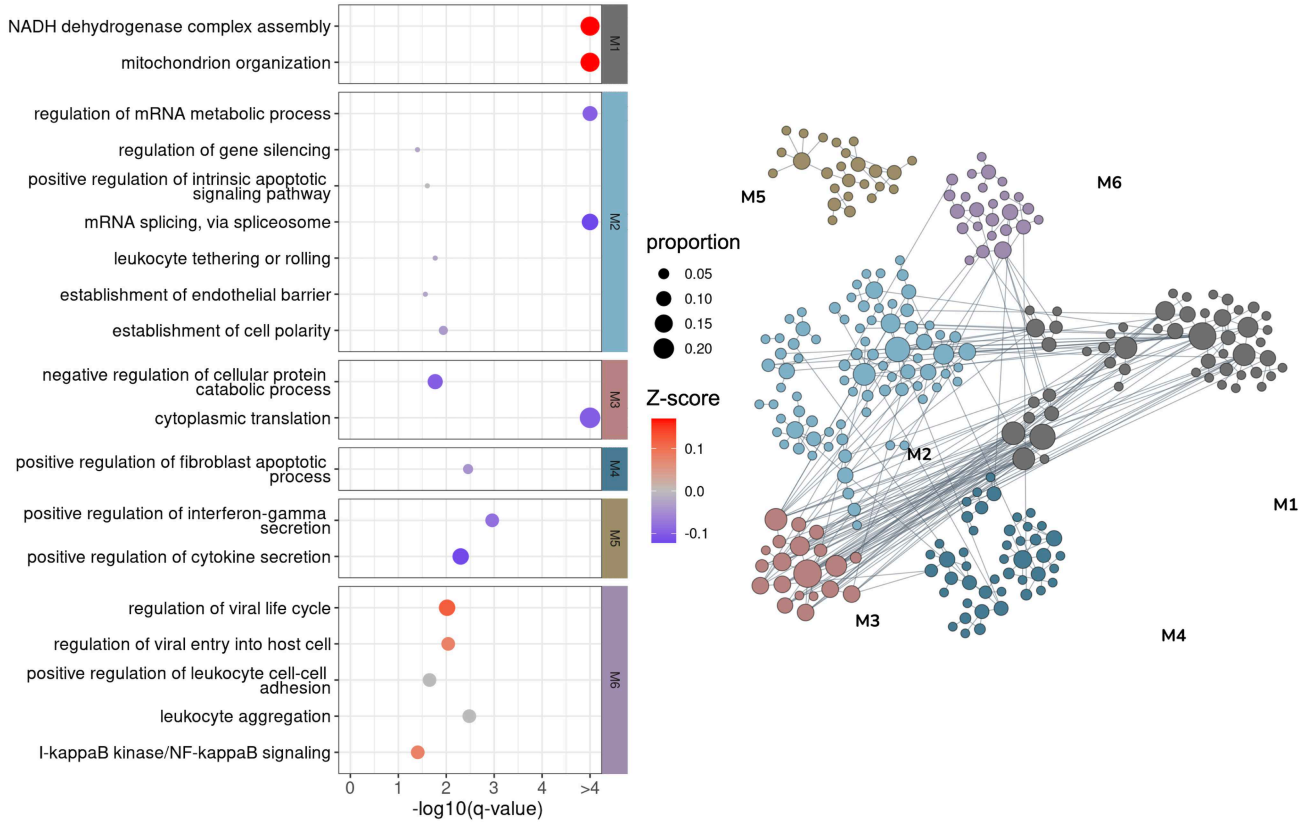

Figure 6. Network-based functional interpretation of common DEGs of MI vs. N and VI vs. N comparisons in CD8+ T cells. The bubble plot (left) shows key pathways enriched in each functional module (M) within the network plot for DEGs common to both MI vs. N and VI vs. N comparisons (right) in (A) $CD8^+$ T cells and (B) NK cells. Left: the color of each bubble represents the Z-score for each pathway which defines the directional tendency of regulation. A positive Z-score is represented by red for up-regulation and a negative Z-score is represented by blue for down-regulation. Bubble size corresponds to the proportion of DEGs in each pathway relative to the total number of DEGs within M. Right: in the network plots, DEGs are clustered into M/gene communities based on functional relatedness in the lung tissue. Each DEG is represented by a node within M and each edge represents a functional association between the pair of DEGs. A node with a larger size reflects a higher degree of connectivity in the network. N: n=4; MI: n=5 and VI: n=4.

NK cells, common DEGs

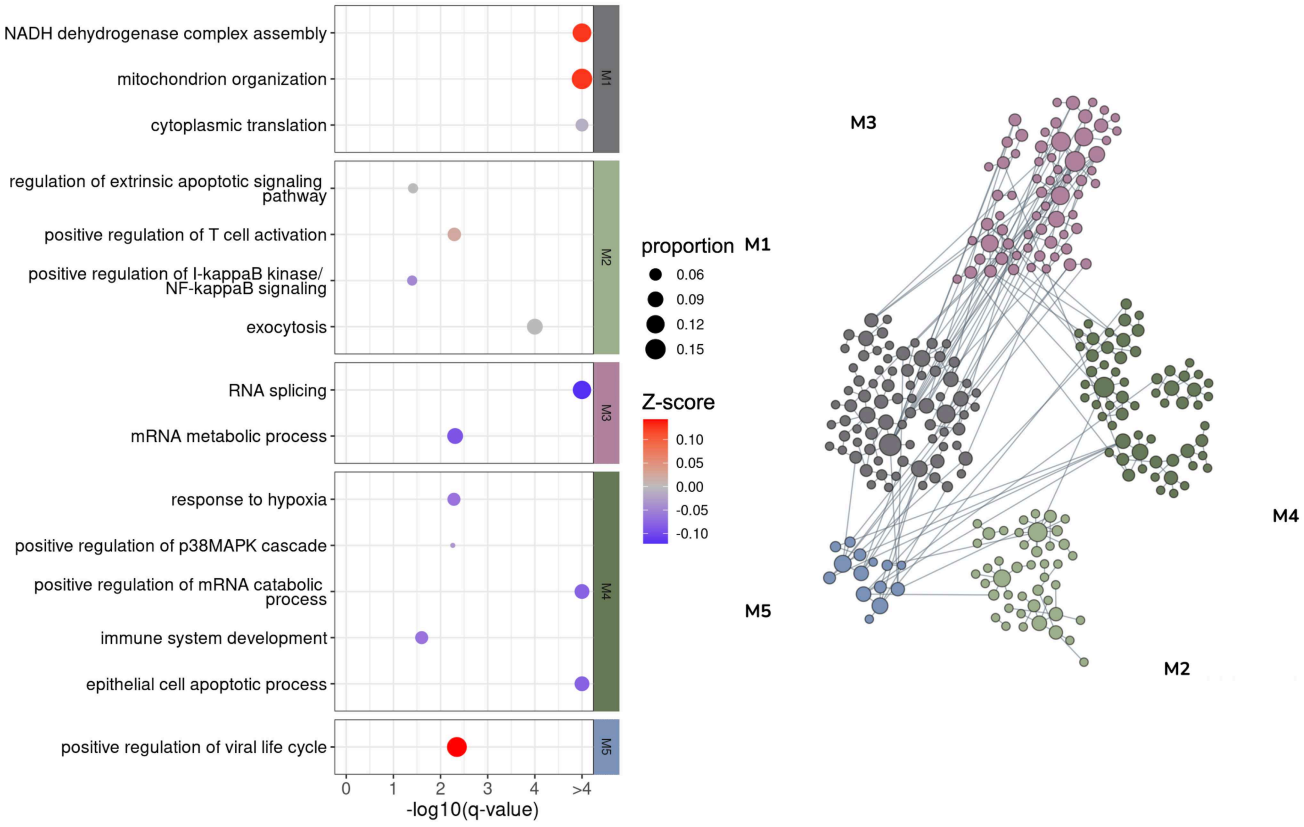

Figure 7. Network-based functional interpretation of common DEGs of MI vs. N and VI vs. N comparisons in NK cells. The bubble plot (left) shows key pathways enriched in each functional module (M) within the network plot for DEGs common to both MI vs. N and VI vs. N comparisons (right) in NK cells. Left: the color of each bubble represents the Z-score for each pathway which defines the directional tendency of regulation. A positive Z-score is represented by red for up-regulation and a negative Z-score is represented by blue for down-regulation. Bubble size corresponds to the proportion of DEGs in each pathway relative to the total number of DEGs within M. Right: in the network plots, DEGs are clustered into M/gene communities based on functional relatedness in the lung tissue. Each DEG is represented by a node within M and each edge represents a functional association between the pair of DEGs. A node with a larger size reflects a higher degree of connectivity in the network. N: n=4; MI: n=5 and VI: n=4.

cDCs, common DEGs

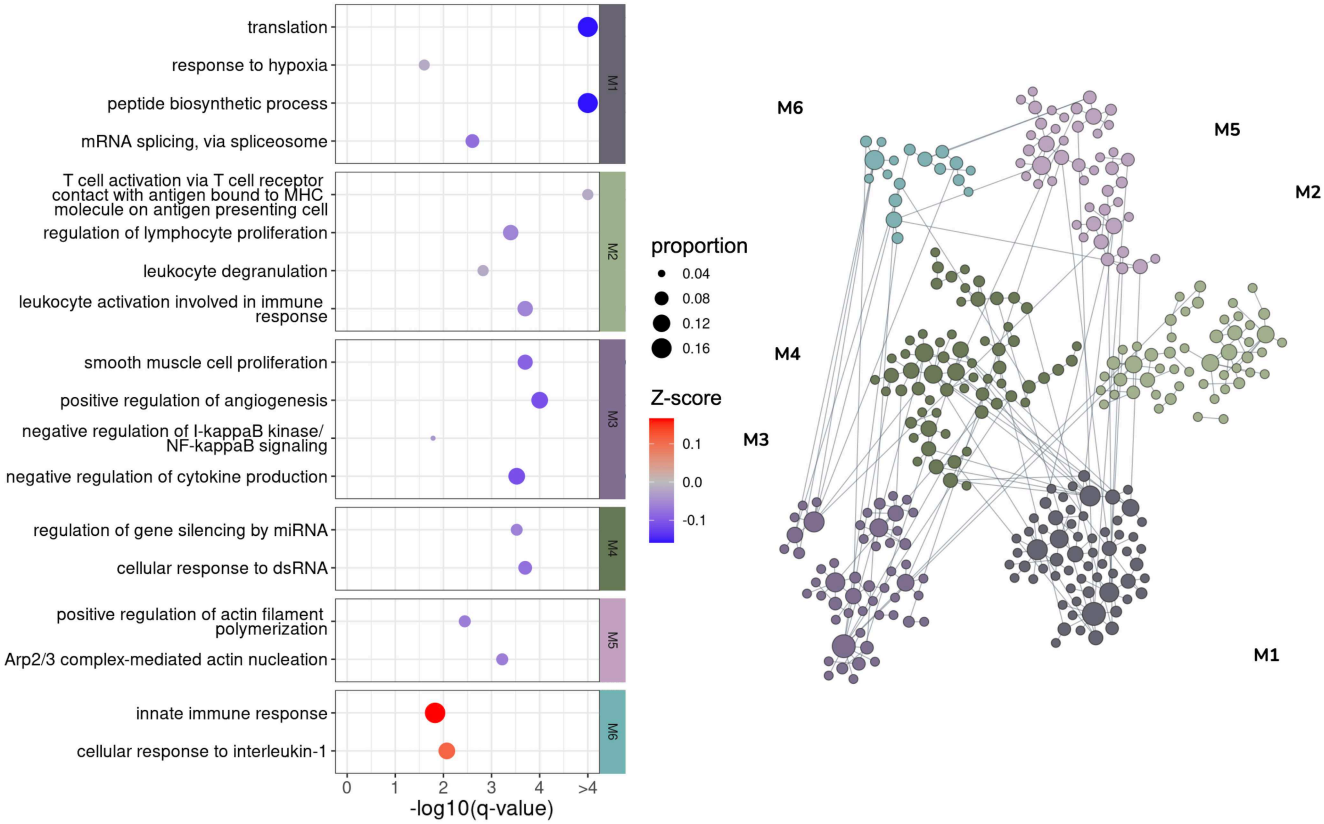

Figure 8. Network-based functional interpretation of DEGs of MI vs. N and VI vs. N comparisons in conventional dendritic cells. The bubble plot (left) shows key pathways enriched in each functional module (M) within the network plot for DEGs common to both MI vs. N and VI vs. N comparisons (right) in cDCs. Left: the color of each bubble represents the Z-score for each pathway which defines the directional tendency of regulation. A positive Z-score is represented by red for up-regulation and a negative Z-score is represented by blue for down-regulation. Bubble size corresponds to the proportion of DEGs in each pathway relative to the total number of DEGs within M. Right: in the network plots, DEGs are clustered into M/gene communities based on functional relatedness in the lung tissue. Each DEG is represented by a node within M and each edge represents a functional association between the pair of DEGs. A node with a larger size reflects a higher degree of connectivity in the network. N: n=4; MI: n=5 and VI: n=4.

Monocytes, common DEGs

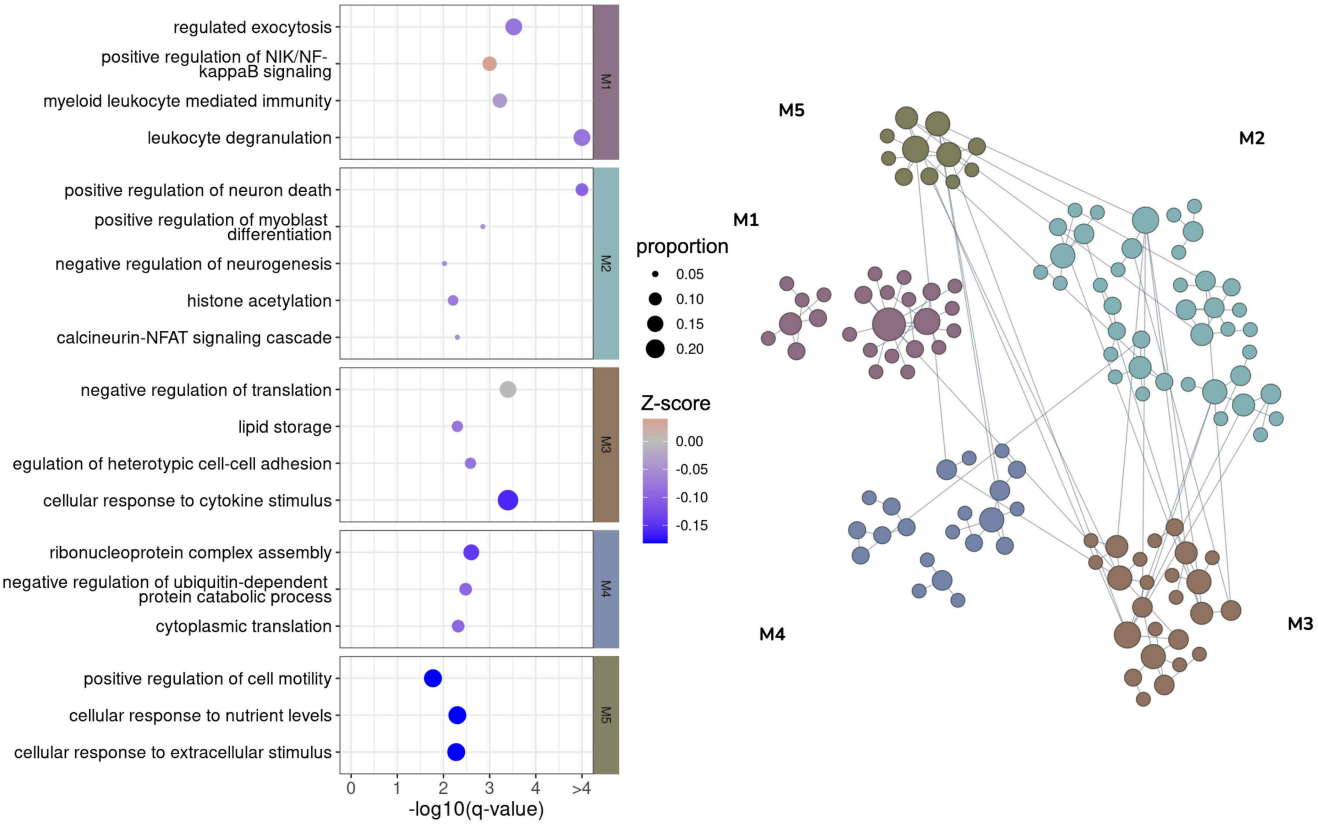

Figure 9. Network-based functional interpretation of DEGs of MI vs. N and VI vs. N comparisons in monocytes. The bubble plot (left) shows key pathways enriched in each functional module (M) within the network plot for DEGs common to both MI vs. N and VI vs. N comparisons (right) in monocytes. Left: the color of each bubble represents the Z-score for each pathway which defines the directional tendency of regulation. A positive Z-score is represented by red for up-regulation and a negative Z-score is represented by blue for down-regulation. Bubble size corresponds to the proportion of DEGs in each pathway relative to the total number of DEGs within M. Right: in the network plots, DEGs are clustered into M/gene communities based on functional relatedness in the lung tissue. Each DEG is represented by a node within M and each edge represents a functional association between the pair of DEGs. A node with a larger size reflects a higher degree of connectivity in the network. N: n=4; MI: n=5 and VI: n=4.